International Journal of Heat and Mass Transfer 91 (2015) 1187–1205

Contents lists available at ScienceDirect

International Journal of Heat and Mass Transfer

journal homepage: www.elsevier.com/locate/ijhmt

# Effects of subcooling and two-phase inlet on flow boiling heat transfer and critical heat flux in a horizontal channel with one-sided and double-sided heating

Chirag R. Kharangate [a], Lucas E. O'Neill [a], Issam Mudawar [a,*], Mohammad M. Hasan [b], Henry K. Nahra [b], Ramaswamy Balasubramaniam [b], Nancy R. Hall [b], Ashley M. Macner [b], Jeffrey R. Mackey [c]

[a] Boiling and Two-Phase Flow Laboratory (BTPFL), School of Mechanical Engineering, Purdue University, 585 Purdue Mall, West Lafayette, IN 47907, USA
[b] NASA Glenn Research Center, 21000 Brookpark Road, Cleveland, OH 44135, USA
[c] Vantage Partners, 3000 Aerospace Parkway, Brook Park, OH 44142, USA

ARTICLE INFO

*Article history:*
Received 13 April 2015
Received in revised form 17 August 2015
Accepted 19 August 2015
Available online 5 September 2015

*Keywords:*
Flow boiling
Critical heat flux
Subcooling
Two-phase inlet
Gravity effects

ABSTRACT

This study explores the influence of inlet subcooling and two-phase inlet on flow boiling heat transfer and critical heat flux in a horizontal 2.5-mm wide by 5-mm high rectangular channel for top wall heating, bottom wall heating and double-sided heating configurations using FC-72 as working fluid. High-speed video imaging is used to identify dominant interfacial characteristics for different combinations of inlet conditions and heating configurations. Three inlet conditions are compared: highly subcooled liquid, slightly subcooled liquid, and saturated two-phase mixture for mass velocities between 205.1 and 3211.6 kg/m$^2$ s. Gravity is shown having a dominant influence on interfacial behavior at low mass velocities below 400 kg/m$^2$ s, while inertia dwarfs gravity effects at high mass velocities around 1600 kg/m$^2$ s. Overall, CHF increases monotonically with increasing inlet subcooling. CHF variation between the three heating configurations is large for low mass velocities and diminishes for high mass velocities. A dimensionless parameter, heat utility ratio, is shown to be an effective means for assessing the influence of subcooling on CHF.



## 1. Introduction

### 1.1. Flow boiling critical heat flux (CHF)

For decades, single-phase thermal management systems have been used to remove heat from temperature sensitive devices in a broad variety of applications. However, as heat fluxes from devices began to escalate, interest has shifted to two-phase thermal management. Examples of these systems include electronic data centers, hybrid vehicle power electronics, avionics, and laser and microwave directed energy systems [1]. The shift to two-phase thermal management is rooted in the ability of these systems to offer orders of magnitude enhancement in heat transfer performance compared to single-phase counterparts. This enhancement is the result of utilization of the coolant's sensible and latent heat content rather than sensible heat alone. With a firm commitment to utilize two-phase thermal management, interest quickly shifted to selecting a suitable two-phase cooling configuration. Simplicity of design and operation, and low cost rendered pool-boiling-based thermosyphons as the primary thermal management solutions for many applications [2,3]. Where pool boiling failed to meet cooling targets, interest shifted to channel flow boiling, including the use of mini/micro-channels, to take advantage of fluid motion to enhance cooling performance [4–6]. And when channel flow boiling could not handle cooling needs, thermal design engineers opted for more aggressive cooling schemes, including jet-impingement [7,8] and spray cooling [9–11]. Recently, there have been efforts to further enhance cooling performance by combining the benefits of different phase-change cooling schemes using hybrid cooling configurations such as micro-channel/jet-impingement cooling [12].

Regardless of which two-phase cooling scheme is selected for a given application, it is essential to maintain nucleate boiling by allowing liquid to replenish the surface of the heat dissipating device to replace the vapor generated by evaporation. The concern here is that intense vapor nucleation, growth and coalescence at high fluxes might culminate in formation of an insulating vapor layer on the surface, which may interrupt bulk

* Corresponding author. Tel.: +1 (765) 494 5705; fax: +1 (765) 494 0539.
*E-mail address:* mudawar@ecn.purdue.edu (I. Mudawar).
*URL:* https://engineering.purdue.edu/BTPFL (I. Mudawar).

http://dx.doi.org/10.1016/j.ijheatmasstransfer.2015.08.059
0017-9310/

**Nomenclature**

| | |
|---|---|
| $b$ | ratio of wetting front length to wavelength |
| $c_p$ | specific heat at constant pressure |
| $D$ | hydraulic diameter of flow channel |
| $G$ | mass velocity |
| $g_e$ | Earth gravity |
| $H$ | height of flow channel's cross-section |
| $h$ | heat transfer coefficient |
| $h_{fg}$ | latent heat of vaporization |
| $H1$ | top heated wall 1 |
| $H2$ | bottom heated wall 2 |
| $L_d$ | development length of flow channel |
| $L_e$ | exit length of flow channel |
| $L_h$ | heated length of flow channel |
| $\dot{m}$ | mass flow rate |
| $P$ | pressure |
| $q''_w$ | wall heat flux |
| $T$ | temperature |
| $t$ | time |
| $T_{in}$ | temperature at inlet to heated portion of channel |
| $T_{sat}$ | saturation temperature |
| $\Delta T_{sub,in}$ | inlet subcooling, $T_{sat} - T_{in}$ |
| $\Delta T_{sub,out}$ | outlet subcooling, $T_{sat} - T_{out}$ |
| $T_w$ | wall temperature |
| $U$ | mean inlet liquid velocity |
| $W$ | width of flow channel and heated walls |
| $x_e$ | thermodynamic equilibrium quality |
| $z$ | axial coordinate |
| $z^*$ | axial location for determining vapor layer thickness and critical wavelength in interfacial lift-off model |

*Greek symbols*

| | |
|---|---|
| $\delta$ | mean thickness of vapor layer |
| $\varepsilon$ | heat utility ratio |
| $\lambda_c$ | critical wavelength |
| $\rho$ | density |
| $\sigma$ | surface tension |

*Subscripts*

| | |
|---|---|
| *avg* | average |
| *c* | critical |
| *d* | developing |
| *e* | exit |
| *f* | saturated liquid; bulk liquid |
| *g* | saturated vapor |
| *h* | heated wall |
| *in* | inlet to heated portion of channel |
| *m* | heated wall nomenclature (1 for $H1$ or 2 for $H2$) |
| *n* | thermocouple location along heated wall |
| *out* | outlet from heated portion of channel |
| *sat* | saturation |
| *sub* | subcooling |
| *w* | wall designation ($H1$ or $H2$) |

liquid access to it. This process is the foundation for occurrence of critical heat flux (CHF), which signals unsteady rise in surface temperature to levels that may cause device overheating or even physical burnout. This is precisely why CHF constitutes the most important design limit for any two-phase thermal management system [13].

### 1.2. Thermal management in future space systems

Thermal management is especially crucial onboard space vehicles, given the complex and varying operating environments of these vehicles. High development and operating costs are also primary concerns when designing a thermal management system for a space application. These costs are highly sensitive to system size and weight. A primary tactic to reducing both is to replace present single-phase thermal management systems with two-phase counterparts in order to capitalize on orders of magnitude enhancement in boiling and condensation heat transfer coefficients compared to single-phase heat transfer. Key targets for implementing two-phase technologies are Thermal Control Systems (TCSs), which are responsible for controlling the temperature and humidity of the operating environment, and Fission Power Systems (FPSs), which are projected to provide both very high power and very low mass to power ratios [14,15].

But application of two-phase technologies in future space missions is thwarted by limited understanding of the influence of reduced gravity on two-phase flow and heat transfer. This need has spurred several reduced gravity collaborative international efforts aimed at exploring all underlying mechanisms, including adiabatic two-phase flow regimes, two-phase pressure drop, flow boiling and condensation heat transfer coefficients, and flow boiling CHF [16].

### 1.3. Single-sided and double-sided heating in a rectangular channel

Of the different boiling schemes, channel flow boiling has received the most attention for space applications because of its simplicity and suitability to thermal management of multiple heat sources. Most prior reduced gravity flow boiling studies have been concentrated on CHF measurement [17,18], particularly in rectangular flow channels that are heated along one side [19,20]. The key reason for relying on single-sided heating is to isolate the effects of reduced or Earth gravity perpendicular to, and parallel to the heated wall.

Fig. 1(a) and (b) depicts flow boiling near CHF at low flow velocities in a horizontal rectangular heated channel with heated top wall and bottom wall, respectively, at 1 $g_e$. These figures illustrate fundamental differences in liquid–vapor interfacial behavior between these two orientations. Top wall heating is shown accumulating vapor against the top wall, culminating in the formation of a thick insulating layer and fairly low CHF. Bottom wall heating benefits from gravity aiding in both vapor removal from the heated wall, and liquid replenishment to the wall. Flow boiling in a horizontal channel that is heated on both top and bottom walls (*i.e.*, double-sided heating) is far more complex, as gravity simultaneously plays a negative role along the top wall, and a positive role along the bottom wall. This behavior is depicted in Fig. 1(c), where the flow boiling behaviors for separately heated top wall, Fig. 1(a), and bottom wall, Fig. 1(b) are more or less superimposed in the same channel. A recent study by Konishi et al. [21,22] involving flow boiling of FC-72 in the microgravity environment of parabolic flight showed double-sided heating provides higher CHF values in comparison with single-sided heating for velocities ranging from 0.1 to 1.9 m/s. This was followed by a study by the present authors [23] involving horizontal FC-72 flow boiling experiments in Earth gravity corresponding to slightly subcooled inlet conditions. These experiments showed that, above a liquid velocity of 1 m/s,

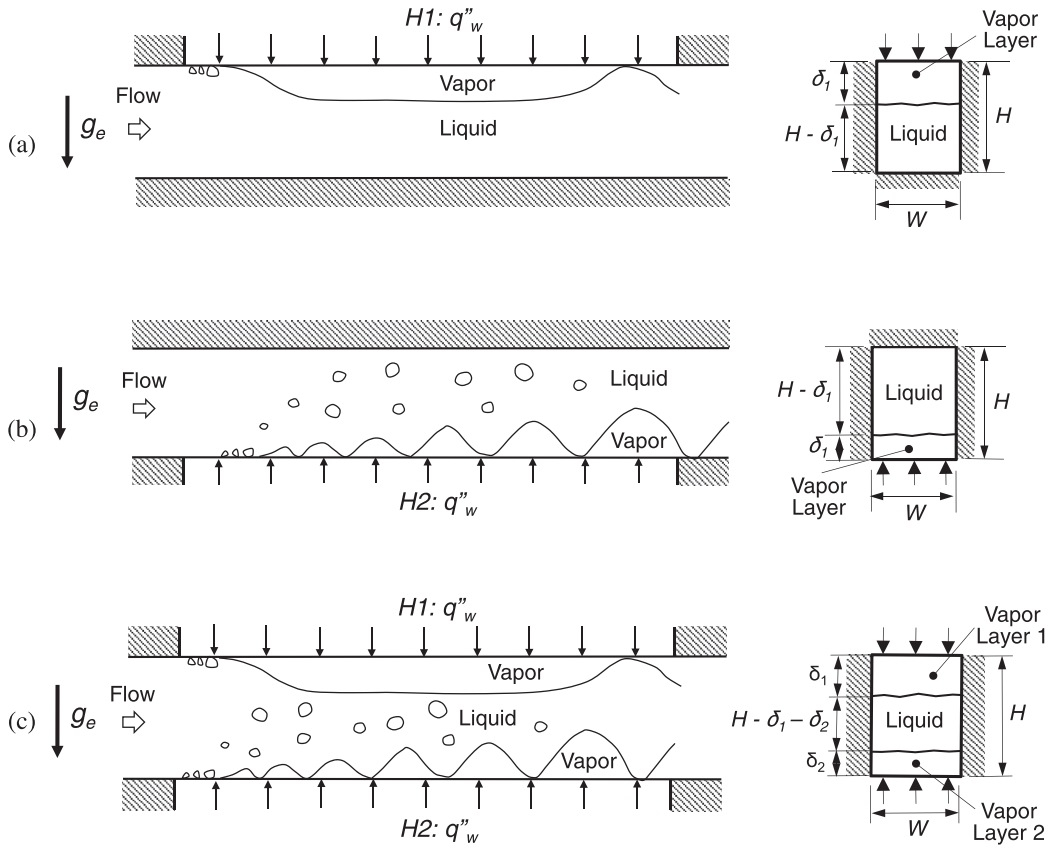


**Fig. 1.** Depiction of horizontal flow boiling near CHF for a rectangular channel with (a) top wall heating, (b) bottom wall heating, and (c) double-sided heating. Adapted from [23].

double-sided heating provides CHF values that are higher than those possible with single-sided heating.

### 1.4. Effects of inlet subcooling and heat utility ratio

Flow boiling heat transfer and CHF are highly dependent on fluid state at the inlet to the flow channel. Three types of inlet conditions are possible: highly subcooled liquid, slightly subcooled liquid, and saturated liquid–vapor mixture. High inlet subcooling enhances CHF appreciably by enabling the coolant to absorb a considerable portion of the wall heat flux in the form of sensible heat instead of by latent heat alone. Strong support for the merits of subcooled inlet conditions over two-phase inlet conditions comes from a number of studies involving single-sided heating in both microgravity [19–22] and Earth gravity [24–27].

To understand the effects of subcooling on flow boiling CHF, it is crucial to quantify the influence of *heat utility ratio*, defined as the ratio of CHF associated with both sensible and latent heat to that with latent heat alone. This is perhaps one of the most challenging endeavors in two-phase heat transfer literature, despite many previous correlative attempts [28–32], where subcooled flow boiling was described as a superposition of single phase forced convection and pool boiling. More recently, Zhang et al. [19] combined experimental results from their own experiments and those of Sturgis and Mudawar [24,25] to develop an empirical correlation for the heat utility ratio.

### 1.5. Objective of study

The present study is a part of a NASA project that was initiated in 2012 with the ultimate goal of developing the Flow Boiling and Condensation Experiment (FBCE) for the International Space Station (ISS). This study is a direct follow-up to a recent study by the authors concerning flow boiling heat transfer and CHF of FC-72 in a rectangular channel [23]. Addressed in this study are the combined complex effects of (i) inlet thermodynamic state (highly subcooled, slightly subcooled or saturated), (ii) mass velocity, and (iii) heating configuration (top wall heating, bottom wall heating and double-sided heating) on both local and spatially averaged heat transfer coefficient and CHF for horizontal flow in Earth gravity. High-speed video imaging is used to capture dominant interfacial patterns for the different combinations of inlet conditions, mass velocity and heating configuration. Finally, the effect of subcooling on CHF is assessed using the aforementioned heat utility ratio.

## 2. Experimental methods

### 2.1. Flow boiling module and heated wall construction

The flow boiling module designed for this study consists mainly of three transparent polycarbonate plastic (Lexan) plates. A 2.5-mm wide and 5.0-mm high rectangular flow channel is milled into the middle Lexan plate as depicted in Fig. 2(a). Slots are milled into the top and bottom Lexan plates to accommodate two 15.5-mm wide, 114.6-mm long and 1.04-mm thick oxygen-free copper heating slabs. O-ring seals are fitted into shallow grooves in the Lexan plates to guard against leaks. The three Lexan plates are sandwiched together between two aluminum support plates. The flow channel features an inlet honeycomb flow straightener followed by an entry length upstream of the heated walls 100 times the hydraulic diameter to ensure fully developed flow. Pressure

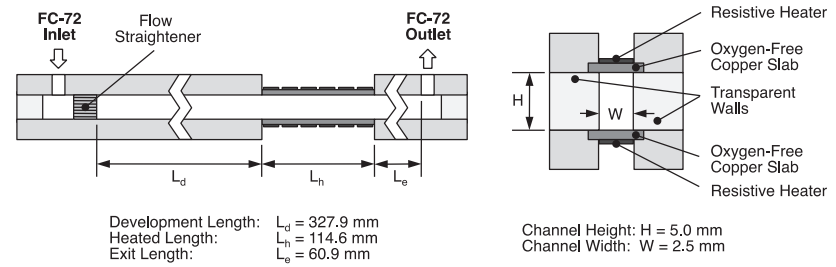


(a)

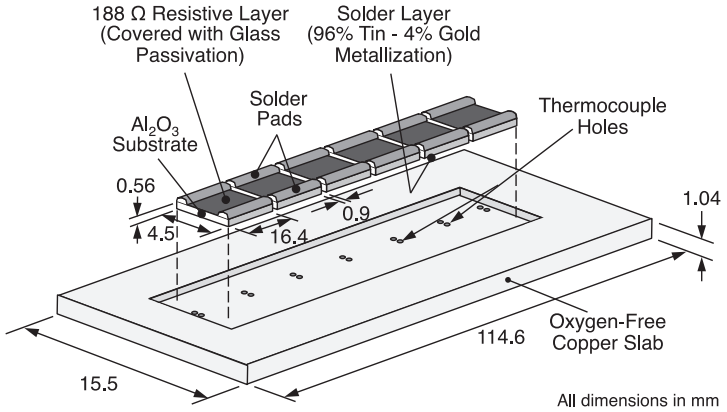


(b)

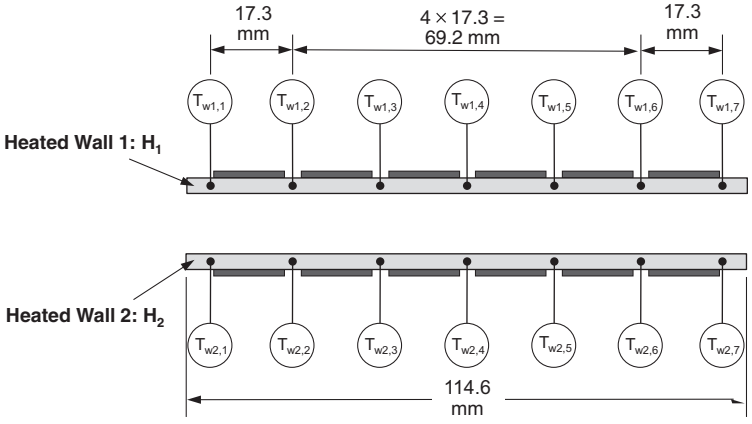


(c)

**Fig. 2.** (a) Key dimensions of the flow channel. (b) Construction of the heated walls and thick-film resistors. (c) Thermocouple layout in the two heated walls.

is measured at the channel inlet, just upstream and just downstream of the copper slabs. Fluid temperature is measured by type-E thermocouples inserted in the channel inlet and exit. Fig. 2(a) shows important dimensions of the flow channel.

The two copper slabs are used as heating walls for the flow channel. Fig. 2(b) and (c) depicts the detailed construction and instrumentation of the walls, respectively. Six 188-Ω, 4.5-mm wide, and 16.4-mm long thick-film resistors are soldered to the back of each copper slab. The resistors are connected electrically in parallel and powered by a variable voltage source to produce uniform heat flux along each wall. A previous study by Zhang et al. [33] showed that a minimum 'asymptotic wall thickness' is necessary to ensure that the measured CHF is both wall thickness independent and representative of real heat exchanger surfaces. For FC-72, they showed that the minimum thickness for a copper surface is 0.40 mm. Using a much larger thickness also has the disadvantage of delaying the attainment of steady state after supplying electrical power to the resistors. Hence, a copper slab thickness of 1.04 mm is adopted in the present study. Each copper slab features two parallel sets of seven shallow holes that are drilled between the resistors for insertion of type-E thermocouples. One set is used to make temperature measurements while the second set is used to trigger an electric relay and cut off power supply to the resistors once CHF is detected. Fig. 2(c) shows axial positions of the measurement thermocouples. The thermocouples are designated as $T_{wm,n}$, where $m$ represents the heated wall (1 for top heated wall $H1$ or 2 for bottom heated wall $H2$), and $n$ the axial thermocouple location.

### 2.2. Two-phase loop

Depicted in Fig. 3, the two-phase loop is constructed to supply FC-72 to the flow boiling module at a prescribed flow rate, pressure and either temperature for subcooled inlet or thermodynamic equilibrium quality for saturated two-phase inlet. The FC-72 is deaerated in a separate degassing facility before being supplied to the flow loop. It is circulated within the loop with the aid of a magnetically coupled gear pump, downstream of which are a filter, Coriolis flow meter, electric pre-heater, and the flow boiling module. Exiting the module, the two-phase mixture passes through a water-cooled condenser to return the fluid to liquid state. An air-pressurized accumulator is situated between the condenser and pump, serving the dual purpose of setting a low pressure reference junction and compensating for any volume expansion or contraction (due to temperature changes or vapor production/collapse) throughout the loop. The entire flow boiling facility, including the flow loop components, data acquisition system, power and instrumentation cabinets, and high-speed camera, are mounted onto an optical table.

### 2.3. Flow visualization techniques

A high-speed camera-link imaging system utilizing a full 10-tap camera-link camera, ATX computer and PCI-Express frame grabber is used to capture the two-phase interfacial features along the heated portion of the flow channel. A fixed frame rate of 2000 frames per second (fps) and pixel resolution of 2040 × 174 are used to capture the entire heated length for each test run. Each video image sequence consists of 3000 frames, or 1.5 s of flow visualization data per test run. Illumination is provided from the back of the flow channel by an array of LEDs, with a light shaping diffuser (LSD) situated between the LEDs and the channel to distribute the light uniformly over the flow channel.

The imaging system is operated using commercial-off-the-shelf (COTS) imaging software provided by the frame grabber company to set the imaging parameters, including the area of interest, exposure time and frame rate. The imaging system is manually triggered to acquire and store the 3000-frame image sequence once the flow boiling achieves steady state. Since each image is 2040 pixel elements × 174 pixel elements × 1 byte, the image occupies approximately 355,960 bytes of memory. At 2000 fps, the image data transfer rate from the camera through the frame grabber and into the host random access memory (RAM) is approximately 710 MB/s. Due to the data bandwidth limitations of the solid-state hard drives (~500 MB/s write speed), image sequences are first buffered to the host RAM before they are saved to a solid-state hard drive for archiving and post-acquisition analysis purposes.

### 2.4. Operating conditions, procedure, and measurement uncertainty

The operating conditions for the study are as follows: FC-72 inlet mass velocity of $G = 205.1–3211.6\ \mathrm{kg/m^2\,s}$, inlet temperature of $T_{in} = 28.4–74.9\ ^\circ\mathrm{C}$ (inlet subcooling of $\Delta T_{sub,in} = 0–31\ ^\circ\mathrm{C}$), inlet equilibrium quality of $x_{e,in} = -0.38$ to 0.18 , and inlet pressure of $P_{in} = 97.1–184.4$ kPa (14.1–26.7 psi). Table 1 provides all details of the data matrix for the present study along with the measured CHF.

For every experiment, an initial waiting period is required to achieve steady state at the inlet to the flow boiling module. Thereafter, data measurements are saved using a Labview program in conjunction with an NI SCXI-1000 data acquisition system. Power to the specific flow boiling heated wall(s) ($H1$, $H2$ or both) is then turned on depending on the prescribed heating configuration for the test. The power is increased in small increments, followed by a waiting period after each increment to achieve steady state, after which the high-speed camera system is triggered to record flow visualization data. The next power increment is then applied and measurements repeated in the same manner. Over the course of a single experiment, the mass flow rate is maintained constant by adjusting pump speed following every power increment. The heated wall relay is set to automatically cut off power supply to the resistors once any of the wall temperatures exceed 130 °C, indicating CHF.

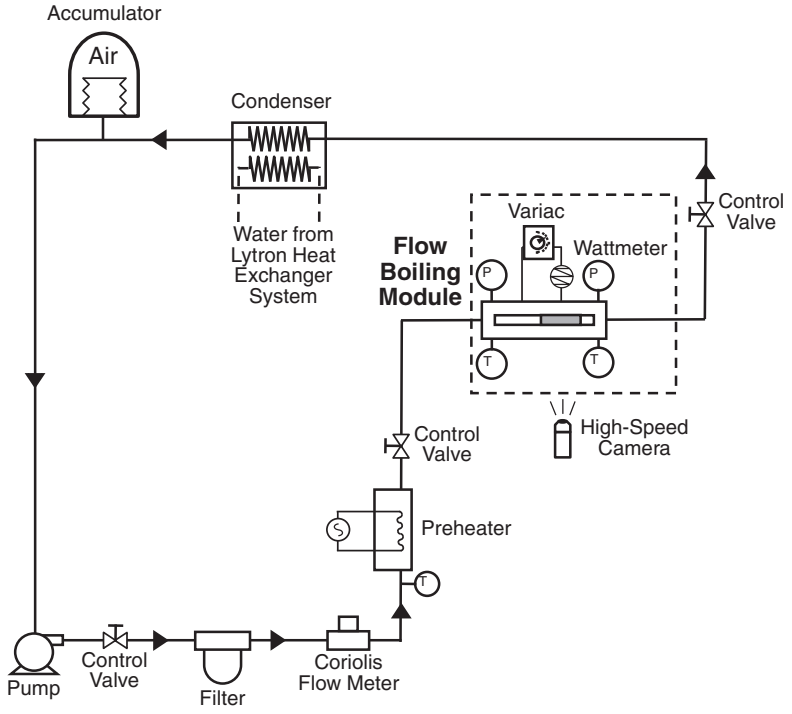


**Fig. 3.** Schematic diagram of the flow loop.

Fluid and heated wall temperatures throughout the facility are measured with type-E thermocouples having an accuracy of ±0.5 °C. STS absolute pressure transducers having an accuracy of ±0.05% are used to measure pressure at several locations along the flow boiling module and the flow loop. The Coriolis flow meter has an accuracy of ±0.1%. The wall heat input is measured with an accuracy of ±0.5 W, and the uncertainty in heat transfer coefficient measurement is ±8%.

## 3. Flow visualization results

Fig. 4(a)–(f) shows individual images of flow boiling along the entire heated portion of the channel for top wall heating, top and bottom wall heating, and bottom wall heating for heat fluxes up to CHF and three different inlet flow conditions: 24.5–25.6 °C subcooling (highly subcooled), 3.3–5.1 °C subcooling (slightly subcooled), and inlet equilibrium quality of 0.03–0.18 (saturated), corresponding to two different mass velocities. Fig. 4(a) and (b) shows images for $G$ = 408.6–469.8 kg/m$^2$ s ($U$ = 0.25–0.29 m/s) and $G$ = 1592.5–1601.3 kg/m$^2$ s ($U$ = 0.98–0.99 m/s), respectively, for the highly subcooled cases. For top wall heating and the lower velocity, Fig. 4(a) shows a wavy vapor layer along the heated wall, with liquid appearing to reach the wall in the wave troughs. Weak flow inertia allows buoyancy to stratify the vapor along the upper wall. For bottom wall heating, Fig. 4(a) shows both discrete and larger coalescent bubbles emanating from the heated wall and projecting toward the opposite wall in the absence of strong flow inertia. This causes bulk liquid to flow downwards, uninterrupted, to compensate for the released vapor, which explains the higher CHF for the bottom heated wall (31.8 W/cm$^2$) compared to the top heated wall (26.3 W/cm$^2$). For double-sided heating, the top wavy vapor layer appears to interrupt the bubble formation, coalescence and liquid return along the bottom wall, which is manifest in a CHF value (18 W/cm$^2$) smaller than that for both top and bottom wall heating. Overall, gravity appears to play a dominant role for this low inertia case.

Fig. 4(b) shows images for similarly high inlet subcooling (24.5–25 °C) but higher mass velocity of $G$ = 1592.5–1601.3 kg/m$^2$ s ($U$ = 0.98–0.99 m/s). Here, higher inertia appears to (i) move boiling activity downstream and (ii) greatly reduce the thickness of the vapor layer along the top heated wall. For bottom wall heating, increased inertia compared to Fig. 4(a) confines boiling activity to the bottom wall. For double-sided heating, the flow appears to combine the vapor behaviors of the top wall and bottom wall heating in the absence of appreciable interaction of top and bottom wall vapor layers. Overall, higher inertia appears to negate much of the gravity-dominated behavior captured in Fig. 4(a), which helps explain why CHF values for all three heating configurations are close to one another. Another important outcome of the combination of higher inertia and high subcooling, which is manifest by confinement of vapor activity to the respective heated walls, is the likelihood of high inequilibrium across the channel, with the liquid saturated near the heated wall and potentially highly subcooled in the core.

Fig. 4(c) and (d) shows images of the flow for $G$ = 394.8–403.4 kg/m$^2$ s ($U$ = 0.25 m/s) and $G$ = 1536.1–1570.3 kg/m$^2$ s ($U$ = 0.97–0.98 m/s), respectively, for low subcooling cases with $\Delta T_{sub,in}$ = 3.3–5.1 °C. For top wall heating and $U$ = 0.25 m/s, Fig. 4(c) shows a wavy vapor layer developing along the top wall and growing in both thickness and wavelength with increasing heat flux. Notice how the downstream of the two wave trough regions, where the liquid contacts the wall, is virtually eliminated at CHF. For bottom wall heating, the influence of gravity is quite apparent, as vapor generated along the bottom wall quickly detaches and moves toward the top wall while being replaced by a downflow of liquid toward the lower wall. While this behavior is also observed in Fig. 4(a) for higher subcooling, the low subcooling in Fig. 4(c) is shown allowing greater vapor production as well as vapor mixing with the bulk liquid, and an appreciable increase in CHF for bottom wall heating compared to top wall heating. High vapor production is also shown inducing significant vapor–liquid mixing in Fig. 4(c) for the double-sided heating. CHF is greatly enhanced with double-sided heating in comparison to top and bottom wall heating because of axial flow acceleration resulting from the increased void fraction. Fig. 4(d) shows flow behavior for $U$ = 0.97–0.98 m/s, where inertia appears to dwarf gravity effects, resulting in more or less similar wavy vapor layer behavior for both top wall heating and bottom wall heating, and the double-sided heating combining vapor behaviors of the two walls when heated separately. Another effect of the inertia dominated flow is a narrower range of CHF values for the three wall heating configurations compared to Fig. 4(c).

Fig. 4(e) and (f) shows images of the flow for $G$ = 396.4–404.1 kg/m$^2$ s and $G$ = 800.6–803.2 kg/m$^2$ s, respectively, for inlet quality ranging from 0.03 to 0.18. With a positive inlet quality, vapor is observed entering the heated portion of the flow channel. For top wall heating at $G$ = 396.4–404.1 kg/m$^2$ s, Fig. 4(e) shows a

**Table 1**
Test cases for study.

| Test case | Heated wall | $U$ (m/s) | $G$ (kg/m$^2$ s) | $x_{e,in}$ | $T_{in}$ (°C) | $P_{in}$ (kPa) | $CHF$ (W/cm$^2$) |
|---|---|---|---|---|---|---|---|
| 1 | Top | 0.18 | 288.6 | −0.38 | 28.6 | 110.5 | 22.0 |
| 2 | Top | 0.29 | 469.8 | −0.31 | 30.1 | 97.1 | 26.3 |
| 3 | Top | 0.52 | 836.8 | −0.34 | 30.5 | 106.7 | 31.0 |
| 4 | Top | 0.98 | 1597.2 | −0.30 | 31.7 | 100.1 | 34.7 |
| 5 | Top | 1.24 | 2004.5 | −0.32 | 31.0 | 103.7 | 38.7 |
| 6 | Top | 1.48 | 2392.1 | −0.34 | 29.8 | 104.9 | 42.9 |
| 7 | Bottom | 0.13 | 205.1 | −0.33 | 28.4 | 98.4 | 29.4 |
| 8 | Bottom | 0.25 | 408.6 | −0.31 | 30.6 | 98.7 | 31.8 |
| 9 | Bottom | 0.49 | 803.0 | −0.31 | 30.8 | 99.3 | 35.6 |
| 10 | Bottom | 0.99 | 1601.3 | −0.30 | 31.8 | 99.0 | 39.5 |
| 11 | Bottom | 1.24 | 2016.1 | −0.32 | 31.0 | 101.8 | 42.3 |
| 12 | Bottom | 1.48 | 2392.4 | −0.34 | 29.9 | 105.2 | 42.3 |
| 13 | Top & Bottom | 0.14 | 226.9 | −0.33 | 28.4 | 98.5 | 12.9 |
| 14 | Top & Bottom | 0.25 | 408.6 | −0.31 | 30.5 | 98.7 | 18.0 |
| 15 | Top & Bottom | 0.49 | 801.3 | −0.32 | 30.6 | 100.2 | 26.1 |
| 16 | Top & Bottom | 0.98 | 1592.5 | −0.31 | 33.2 | 105.6 | 37.1 |
| 17 | Top & Bottom | 1.24 | 2007.5 | −0.33 | 32.3 | 109.1 | 42.6 |
| 18 | Top & Bottom | 1.47 | 2386.3 | −0.33 | 30.7 | 105.6 | 42.6 |
| 19 | Top | 0.13 | 216.4 | −0.07 | 56.4 | 119.7 | 6.9 |
| 20 | Top | 0.25 | 403.4 | −0.05 | 58.9 | 122.0 | 9.3 |
| 21 | Top | 0.50 | 797.4 | −0.05 | 60.1 | 127.5 | 17.2 |
| 22 | Top | 0.75 | 1204.0 | −0.07 | 60.5 | 133.3 | 21.0 |
| 23 | Top | 0.98 | 1570.3 | −0.05 | 62.6 | 136.3 | 23.1 |
| 24 | Top | 2.02 | 3200.2 | −0.06 | 67.2 | 161.5 | 31.0 |
| 25 | Bottom | 0.13 | 208.0 | −0.10 | 56.8 | 130.1 | 27.1 |
| 26 | Bottom | 0.25 | 400.5 | −0.07 | 59.1 | 128.7 | 28.2 |
| 27 | Bottom | 0.50 | 804.6 | −0.05 | 60.6 | 130.5 | 29.4 |
| 28 | Bottom | 0.75 | 1192.7 | −0.07 | 60.5 | 136.0 | 28.2 |
| 29 | Bottom | 0.98 | 1567.4 | −0.05 | 62.5 | 137.6 | 28.2 |
| 30 | Bottom | 2.02 | 3199.3 | −0.06 | 66.9 | 161.8 | 31.8 |
| 31 | Top & Bottom | 0.13 | 206.5 | −0.09 | 57.7 | 128.4 | 8.6 |
| 32 | Top & Bottom | 0.25 | 394.8 | −0.07 | 59.5 | 129.7 | 18.0 |
| 33 | Top & Bottom | 0.50 | 793.3 | −0.07 | 60.2 | 134.2 | 25.0 |
| 34 | Top & Bottom | 0.75 | 1196.5 | −0.09 | 61.5 | 144.6 | 28.4 |
| 35 | Top & Bottom | 0.97 | 1536.1 | −0.07 | 64.0 | 150.2 | 29.6 |
| 36 | Top & Bottom | 1.52 | 2409.0 | −0.09 | 64.7 | 162.1 | 32.0 |
| 37 | Top & Bottom | 2.04 | 3211.6 | −0.10 | 67.7 | 177.1 | 33.2 |
| 38 | Top | | 400.3 | 0.18 | 65.1 | 138.0 | 12.2 |
| 39 | Top | | 803.1 | 0.08 | 66.8 | 142.4 | 18.1 |
| 40 | Top | | 1599.7 | 0.04 | 73.4 | 170.8 | 25.2 |
| 41 | Bottom | | 396.4 | 0.18 | 65.9 | 143.0 | 27.1 |
| 42 | Bottom | | 802.0 | 0.03 | 64.9 | 139.5 | 23.8 |
| 43 | Bottom | | 1592.9 | 0.04 | 74.0 | 173.4 | 26.0 |
| 44 | Top & Bottom | | 404.1 | 0.17 | 65.4 | 141.0 | 16.2 |
| 45 | Top & Bottom | | 800.6 | 0.07 | 68.1 | 149.7 | 24.0 |
| 46 | Top & Bottom | | 1592.6 | 0.03 | 74.9 | 184.4 | 26.1 |

very thick wavy vapor layer, consisting of both the incoming vapor and the vapor generated by heating, propagating along the top wall. The thickness of the vapor layer increases with increasing heat flux until the vapor appears to engulf the entire cross-section at CHF. For bottom wall heating, high flow acceleration resulting from the large void fraction confines vapor activity to the bottom wall. This implies that the dominant role of gravity observed in Fig. 4(a) and (c) is greatly compromised with saturated inlet conditions. For double-sided heating, a three-layer separated flow is established with wavy vapor layers covering both top and bottom walls, and a middle liquid layer in between. Notice that the top wall vapor layer is much thicker than the bottom wall vapor layer. This can be explained by buoyancy effects accumulating both incoming and generated vapor toward the top wall. Fig. 4(f) shows flow behavior for $G = 800.6–803.2$ kg/m$^2$ s and $x_{e,in} = 0.03–0.08$. A lower inlet quality for this case compared to Fig. 4(e) is shown reducing the amount of incoming vapor. There is also better symmetry in wavy vapor layer development along the top heated and bottom heated walls because of the high mass velocity. Additionally, high inertia helps achieve closer CHF values for the three wall heating configurations in Fig. 4(f) compared to those in Fig. 4(e).

Fig. 5 shows 15 sequential images of the flow spaced 1.5 ms apart at 74–86% CHF for top wall heating (with only $H1$ on), for $G = 400.3–1597.2$ kg/m$^2$ s ($U = 0.25–0.98$ m/s) and three types of inlet conditions: highly subcooled, slightly subcooled, and saturated. For high inlet subcooling of $\Delta T_{sub,in} = 25.6$ °C and $U = 0.29$ m/s, bubble nucleation commences downstream of the inlet, and the bubbles coalesce into a wavy vapor layer. Increasing the velocity to $U = 0.98$ m/s for the same high subcooling greatly reduces the thickness of the vapor layer. For low inlet subcooling of $\Delta T_{sub,in} = 3.6$ °C, bubbles are seen nucleating closer to the inlet and coalescing into a thick wavy vapor layer. Increasing the velocity to $U = 0.98$ m/s for similarly small inlet subcooling decreases the wavelength of the vapor layer while increasing the number of wetting fronts in between. For saturated inlet conditions with $x_{e,in} = 0.08–0.17$, the vapor layer is initiated at the inlet where it is fed by the incoming vapor. The combination of incoming vapor and the vapor generated due to heating results in a comparatively very thick vapor layer along the top heated wall.

Fig. 6 shows 15 sequential images of the flow spaced 1.5 ms apart at 75–85% CHF for bottom wall heating (with only $H2$ on) for $G = 396.4–1601.3$ kg/m$^2$ s ($U = 0.25–0.99$ m/s) and three types of inlet conditions: highly subcooled, slightly subcooled, and saturated. For high inlet subcooling of $\Delta T_{sub,in} = 25.5$ °C and $U = 0.25$ m/s, small vapor bubbles are seen forming upstream and both growing and coalescing as they propagate along the bottom wall. Relatively weak inertia allows gravity to draw the vapor across the channel toward the top wall. Some of these bubbles are seen to condense in the highly subcooled liquid. For a similar subcooling and a higher velocity of $U = 0.99$ m/s, the vapor formation is pushed farther downstream and the vapor layer is much thinner and, because of the high inertia, well confined to the lower wall. For low inlet subcooling of $\Delta T_{sub,in} = 5.1$ °C and $U = 0.25$ m/s, a

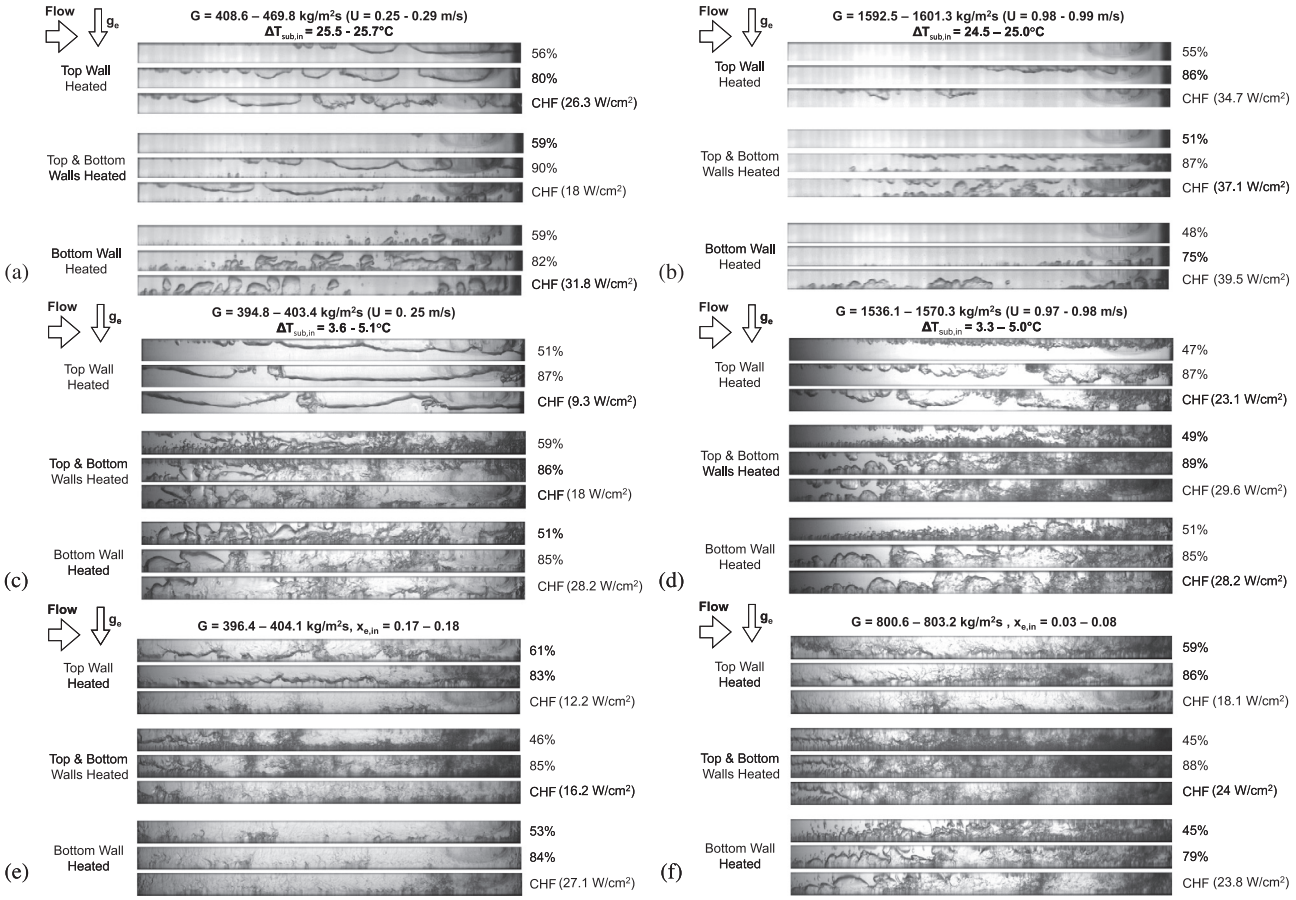


**Fig. 4.** Variations of interfacial behavior with increasing heat flux for top wall heating, double-sided heating, and bottom wall heating for (a) $G = 408.6–469.8$ kg/m$^2$ s and $\Delta T_{sub,in} = 25.5–25.7$ °C, (b) $G = 1592.5–1601.3$ kg/m$^2$ s and $\Delta T_{sub,in} = 24.5–25.0$ °C, (c) $G = 394.8–403.4$ kg/m$^2$ s and $\Delta T_{sub,in} = 3.6–5.1$ °C, (d) $G = 1536.1–1570.3$ kg/m$^2$ s and $\Delta T_{sub,in} = 3.3–5.0$ °C, (e) $G = 396.4–404.1$ kg/m$^2$ s and $x_{e,in} = 0.17–0.18$, and (f) $G = 800.6–803.2$ kg/m$^2$ s and $x_{e,in} = 0.03–0.08$.

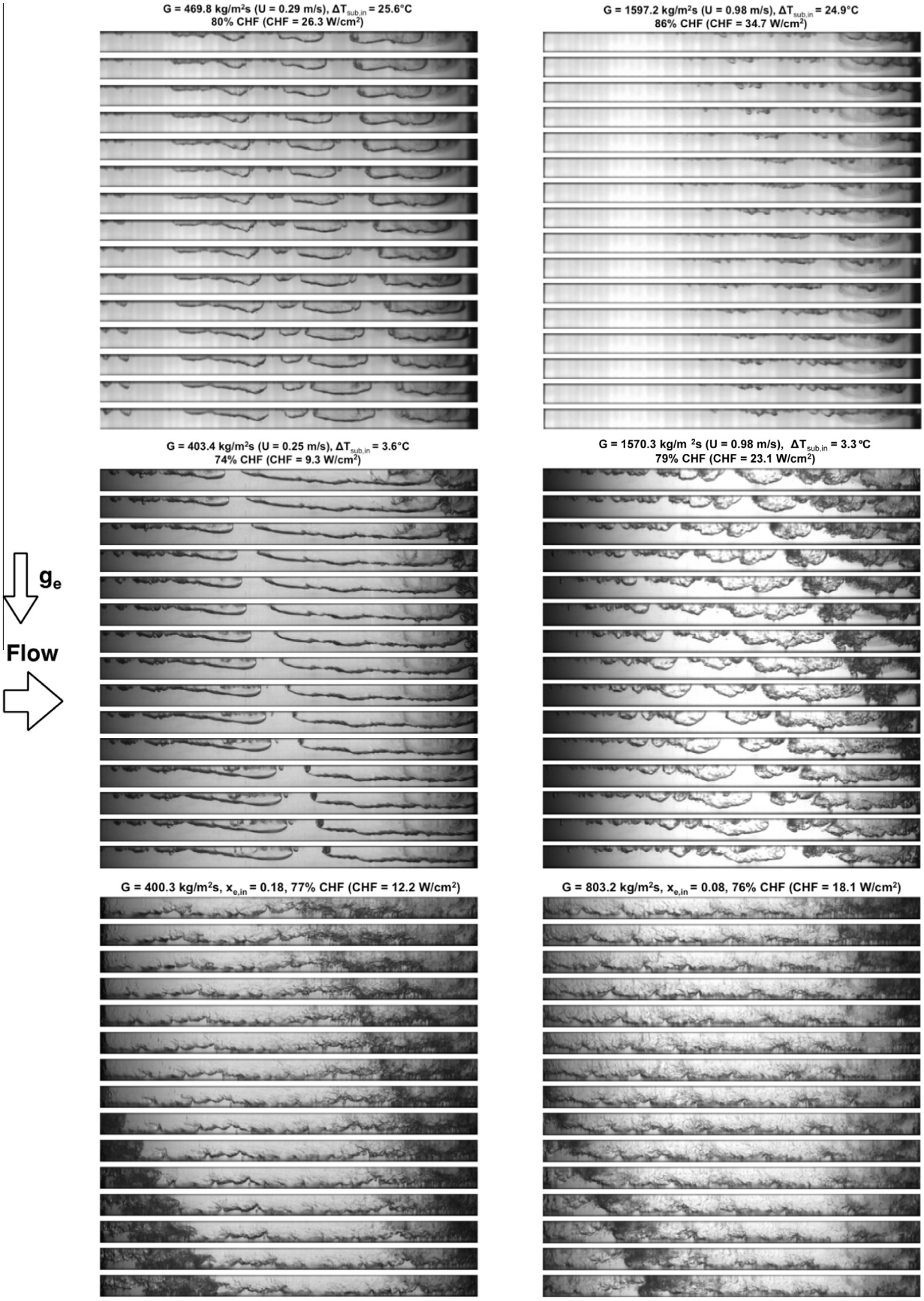


**Fig. 5.** Sequential high-speed video images from top wall heating experiments for different mass velocities, inlet subcoolings, and inlet qualities.

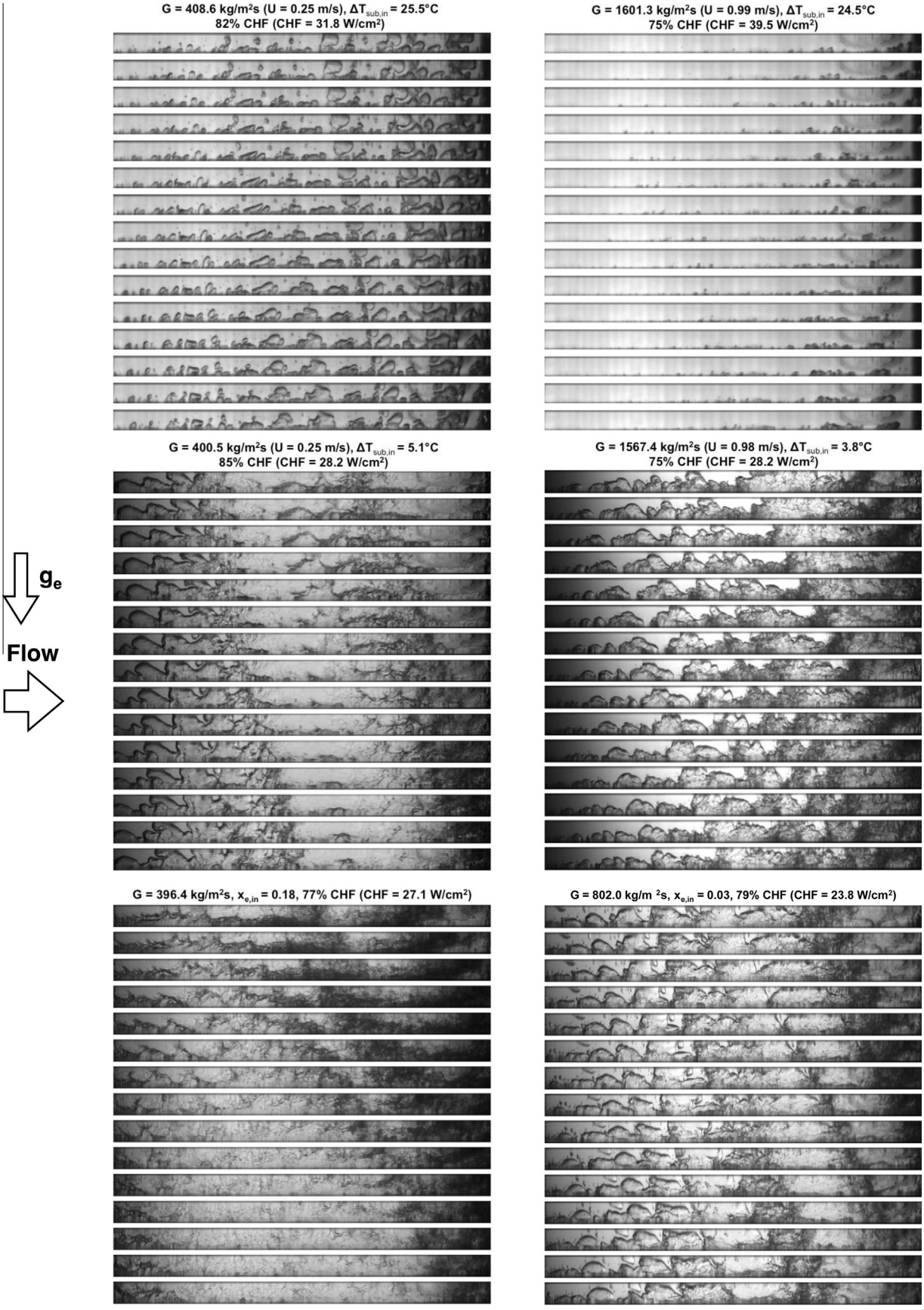


**Fig. 6.** Sequential high-speed video images from bottom wall heating experiments for different mass velocities, inlet subcoolings and inlet qualities.

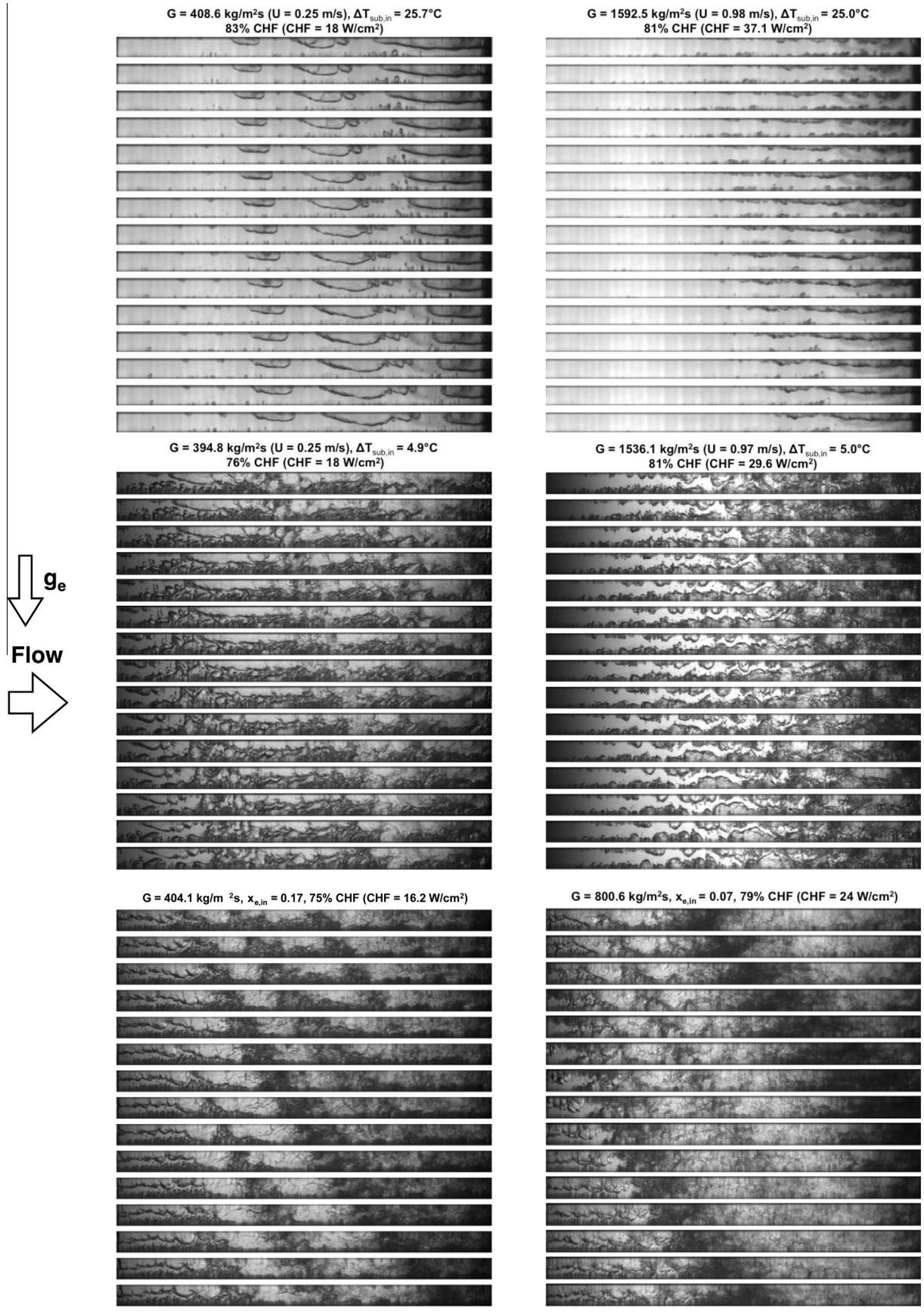


**Fig. 7.** Sequential high-speed video images from double-sided heating experiments for different mass velocities, inlet subcoolings, and inlet qualities.

thick vapor layer is seen forming along the bottom wall growing in thickness while approaching the top wall. Increasing the velocity to $U = 0.98$ m/s for a similarly low inlet subcooling increases the importance of inertia relative to buoyancy, which is manifest by a lesser tendency of the bottom wall's vapor layer to reach the top wall. For saturated inlet conditions with $x_{e,in} = 0.03–0.18$, the flow is comprised of three layers at the inlet as described by Kharangate et al. [26], with a very thin top layer of incoming vapor, a middle liquid layer and the newly generated vapor layer along the bottom wall. This behavior is less discernible downstream because of the high vapor void fraction.

Fig. 7 shows 15 sequential images spaced 1.5 ms apart at 75–83% CHF for double-sided heating (with $H1$ and $H2$ simultaneously turned on) for $G = 394.8–1592.5$ kg/m$^2$ s ($U = 0.25–0.98$ m/s) and the three types of inlet conditions: highly subcooled, slightly subcooled, and saturated. For high inlet subcooling of $\Delta T_{sub,in} = 25.7$ °C and $U = 0.25$ m/s, there are clear differences in vapor formation along the top and bottom walls. For the bottom wall, small bubbles are generated along the bottom wall, which, because of relatively strong gravity effects at this low velocity, travel across toward the top wall where they accumulate into the top walls' wavy vapor layer. Increasing the velocity to $U = 0.98$ m/s for the same high inlet subcooling strengthens inertia relative to gravity, which is manifest by thinner vapor layers and lessened vapor accumulation along the top wall. For low inlet subcooling of $\Delta T_{sub,in} = 4.9$ °C and $U = 0.25$ m/s, the flow appears to combine the vapor layer behaviors exhibited by the two walls when heated separately as shown in Figs. 5 and 6 for similar inlet conditions. Increasing the velocity to $U = 0.97$ m/s for a similarly low inlet subcooling results in wavy vapor layers along the top and bottom walls exhibiting a wavy 'meshing' behavior, where the wave peak from one of the heated walls grows toward the trough (wetting front) between two wave peaks on the opposite wall, which is reminiscent of gear meshing as discussed by Konishi et al. [21,22] for flow boiling in microgravity at $U = 0.1–1.9$ m/s. For saturated inlet conditions with $x_{e,in} = 0.07–0.17$, vapor enters the heated portion of the channel attached to the top wall. This causes large differences between the thicknesses of the top and bottom layers, especially for the lower mass velocity of $G = 404.1$ kg/m$^2$ s.

## 4. Experimental results

### 4.1. CHF trends

Fig. 8(a) shows the variation of CHF with mass velocity for top wall heating, bottom wall heating, and double-sided heating configurations and the three inlet conditions of highly subcooled ($\Delta T_{sub,in} = 24.5–31$ °C), slightly subcooled ($\Delta T_{sub,in} = 3.3–7.7$ °C), and saturated ($x_{e,in} = 0.03–0.18$).

For the low subcooling and saturated inlet cases, CHF for $G < 800$ kg/m$^2$ s is lowest for top wall heating due to vapor accumulation along the top wall by the relatively strong buoyancy

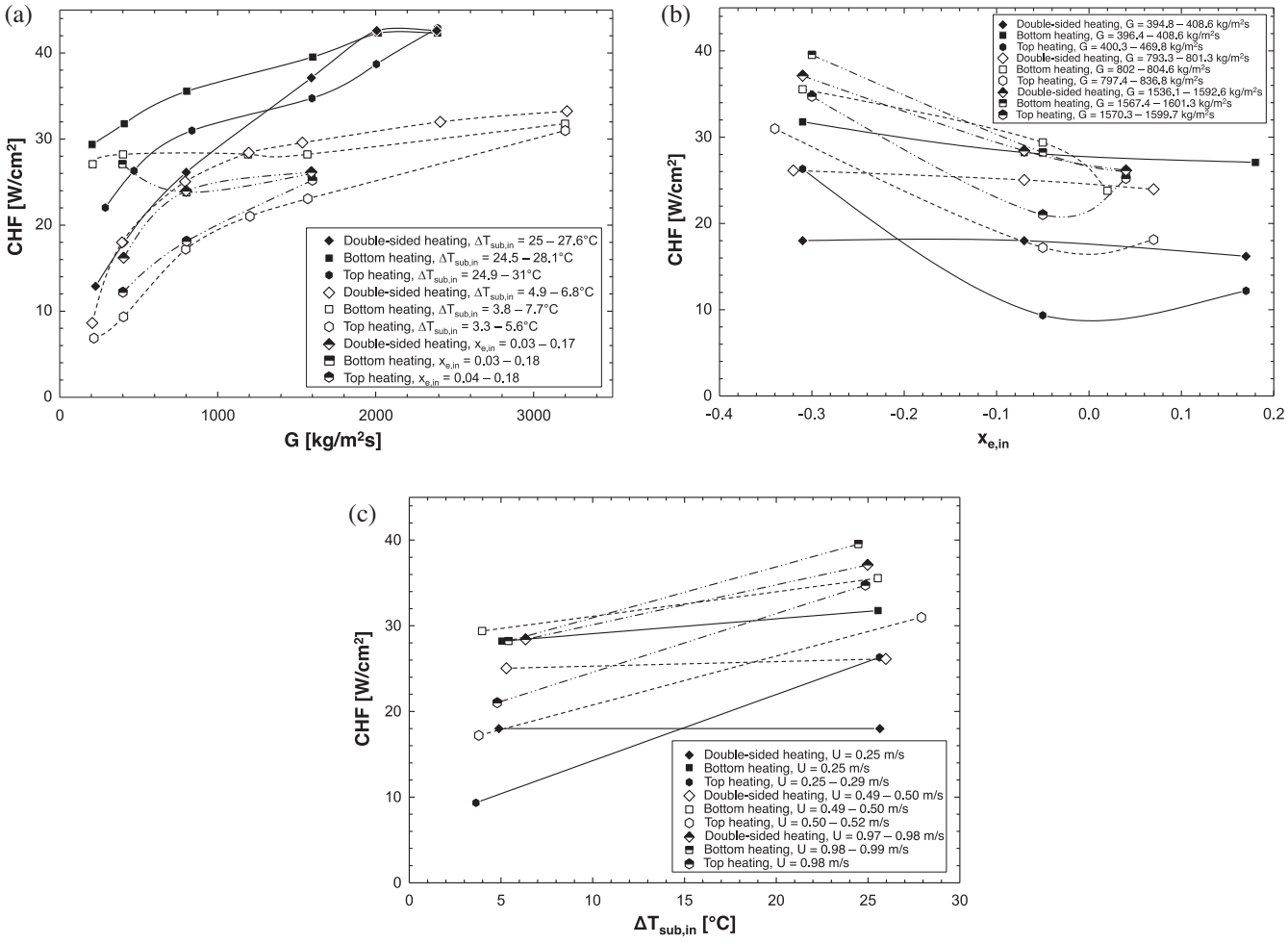


**Fig. 8.** Variations of CHF with (a) mass velocity, (b) inlet quality, and (c) inlet subcooling for top wall heating, bottom wall heating and double-sided heating.

effects as observed in Fig. 4(c) and (e). Also for $G < 800$ kg/m$^2$ s, bottom wall heating is shown to yield the highest CHF because of the strong buoyancy effects that assist vapor removal from the bottom heated wall toward the top unheated wall and increase mixing as well as bulk liquid access to the bottom heated wall. For the low subcooling and saturated inlet cases, double-sided heating yields CHF values for $G < 800$ kg/m$^2$ s that are in between those for top wall heating and bottom wall heating. The double-sided configuration could be viewed as a superposition of the two other heating configurations. For low inlet subcooling ($\Delta T_{sub,in} = 3.3$–$7.7$ °C) and $G > 1600$ kg/m$^2$ s, double-sided heating outperforms the other two configuration. As shown earlier in Fig. 4(d), this inertia dominated range tends to confine vapor production during double-sided heating to the individual walls, while also capitalizing on the heat transfer enhancement resulting from greater axial flow acceleration compared to individually heated walls. Notice also for low inlet subcooling that CHF values for all three heating configurations converge around $G = 3200$ kg/m$^2$ s, where the vapor layers become quite thin and axial acceleration quite low. For saturated inlet ($x_{e,in} = 0.03$–$0.18$), CHF values for all three heating configurations converge around 1600 kg/m$^2$ s. With respect to the high inlet subcooling ($\Delta T_{sub,in} = 24.5$–$31$ °C) cases, Fig. 8(a) also shows that bottom wall heating outperforms the other heating configurations for lower mass velocities, in this case $G < 1600$ kg/m$^2$ s. However, unlike the low subcooling and saturated inlet cases, CHF for double-sided heating is lower than for top wall heating for $G < 1600$ kg/m$^2$ s. This behavior can be explained by examining Fig. 4(a), which shows double-sided heating allowing vapor generated from the bottom wall to accumulate along the top wall, resulting in further thickening of the top wall vapor layer. Convergence of CHF values for the three heating configurations for the high subcooling cases occurs around $G = 2400$ kg/m$^2$ s. Overall, it is worth noting that flow acceleration is low for high subcooling, which may explain some of the

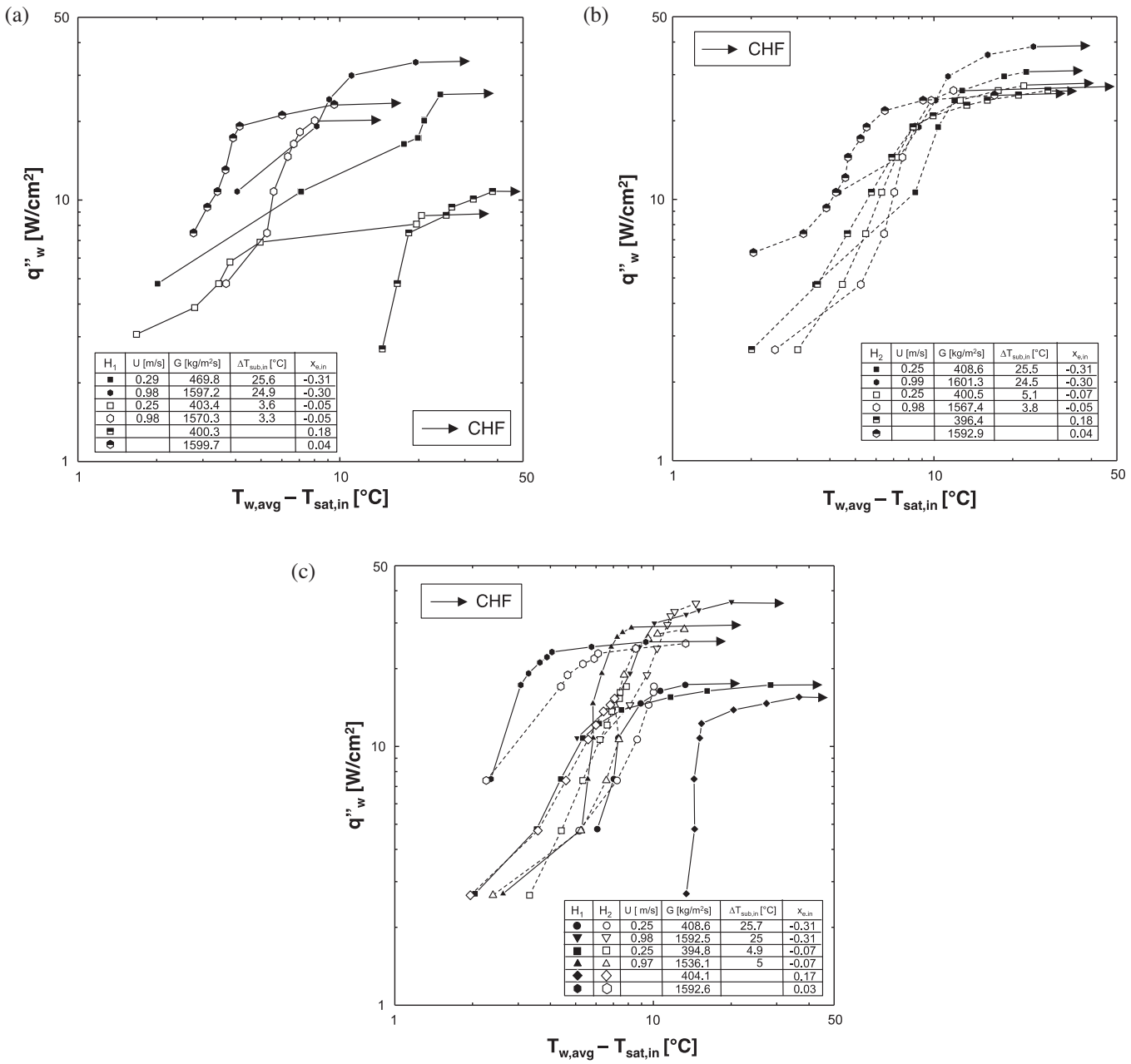


**Fig. 9.** Boiling curves for different mass velocities, inlet subcoolings, and inlet qualities for (a) top wall heating, (b) bottom wall heating, and (c) double-sided heating.

differences in CHF trends between high subcooling cases on one hand and both low subcooling and saturated cases on the other.

Fig. 8(b) shows the variation of CHF with inlet equilibrium quality, $x_{e,in}$, for top wall heating, bottom wall heating, and double-sided heating configurations, and mass velocities of $G = 394.6–469.8$ kg/m$^2$ s, 793.3–836.8 kg/m$^2$ s and 1536.1–1601.3 kg/m$^2$ s. In the subcooled region where $x_{e,in} < 0$, CHF is seen to decrease monotonically with increasing $x_{e,in}$, (*i.e.*, decreasing inlet subcooling). Bottom heating and double-sided heating show CHF continuing to decrease with increasing $x_{e,in}$ for $x_{e,in} > 0$, which is to be expected since reduced liquid content decreases the energy required to trigger CHF. However, top wall heating does not follow this trend and CHF increases with increasing $x_{e,in}$ for $x_{e,in} > 0$. This reversal in trend relative to the two other heating configurations can be explained by the high positive $x_{e,in}$ values producing appreciable flow acceleration, which increase inertia compared to gravity effects, eliminating the detrimental effects of vapor accumulation along the top wall.

Fig. 8(c) shows the variation of CHF with inlet subcooling for only the highly subcooled and slightly subcooled cases. CHF increases monotonically with increasing subcooling for all cases because of the need to overcome the liquid's increasing sensible heat deficiency prior to evaporation. CHF variations among the three different heating configurations for a given velocity are consistent with those of CHF versus $x_{e,in}$ for $x_{e,in} < 0$ in Fig. 8(b).

### 4.2. Flow boiling curves

As shown earlier in Fig. 2(c), the heated walls are fitted each with seven thermocouples for wall temperature measurements. The temperatures are designated as $T_{w1,n}$ and $T_{w2,n}$, where 1 and 2 refer to top heated wall *H*1 and bottom heated wall *H*2, respectively, and *n* thermocouple axial location along the respective heated wall. Fig. 9(a) and (c) shows boiling curves for $G = 394.8–1601.3$ kg/m$^2$ s ($U = 0.25–0.99$ m/s) for top wall heating, bottom wall heating, and double-sided heating, respectively, for highly subcooled, slightly subcooled and saturated inlet conditions. The wall heat flux, $q''_w$, is plotted against the difference between average wall temperature, $T_{w,avg}$, and inlet saturation temperature, $T_{sat,in}$. All curves exhibit trends observed in a typical boiling curve, with the slope increasing as the flow transitions from single phase to nucleate boiling, then decreasing sharply just before CHF. However, the transition points differ for different inlet conditions

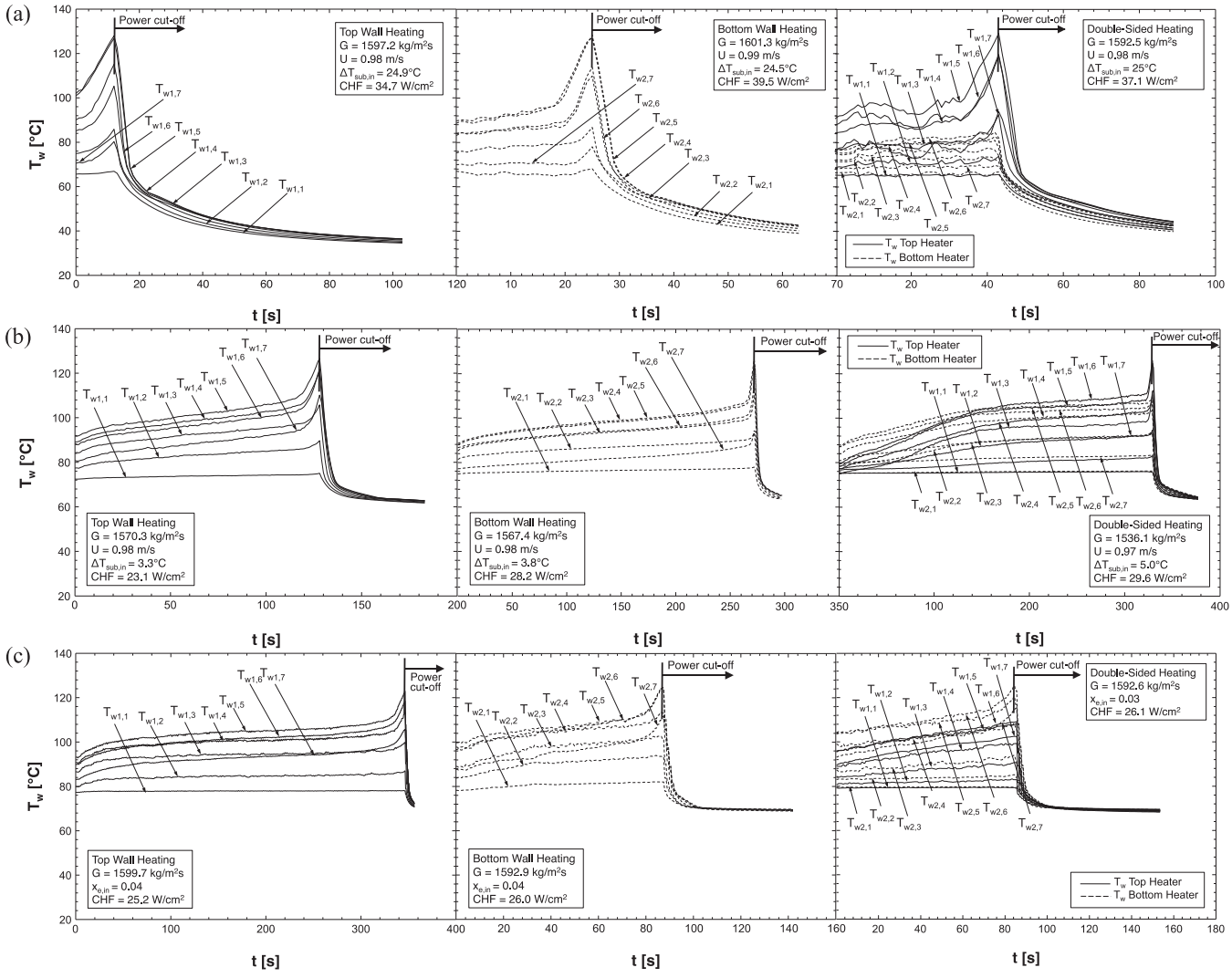


**Fig. 10.** Temporal records of wall thermocouples during CHF transient for different mass velocities and top wall heating, bottom wall heating, and double-sided heating for (a) $\Delta T_{sub,in} = 24.5–25$ °C, (b) $\Delta T_{sub,in} = 3.3–5.0$ °C, and (c) $x_{e,in} = 0.03–0.04$.

and heating configurations. For top wall heating and high inlet subcooling of $\Delta T_{sub,in}$ = 24.9–25.6 °C, Fig. 9(a) shows increasing $G$ from 469.8 to 1597.2 kg/m$^2$ s shifts the entire boiling curve upwards. An even more profound upward shift in the boiling curve is achieved with increasing $G$ for both low inlet subcooling of $\Delta T_{sub,in}$ = 3.3–3.6 °C and saturated inlet with $x_{e,in}$ = 0.04–0.18. Increased sensitivity to $G$ with low subcooling and saturated inlet conditions reflects the strong negative influence of gravity in the form of substantial thickening of the vapor layer along the top wall for low $G$, compared to a more inertia dominated flow thinning the same vapor layer for high $G$. For bottom wall heating, Fig. 9(b) shows overall trends similar to those for top wall heating, with the main difference that the overall influence of $G$ is abated compared to Fig. 9(a), especially for the low subcooling and saturated inlet conditions. For double-sided heating, Fig. 9(c), where the flow is influenced by vapor layer development along both walls, the effect of $G$ is exacerbated as for top wall heating, Fig. 9(a). This effect is most pronounced for the saturated inlet cases with $x_{e,in}$ = 0.03–0.17. Another observation in Fig. 9(c) is that the boiling curves for the individual walls in the double-sided configuration are more or less reflective of trends of same walls in single-sided heating configurations, Fig. 9(a) and (b). A notable difference for double-sided heating versus both top wall and bottom wall heating is a steeper slope in the nucleate boiling region, which, as discussed earlier, is a reflection of greater flow acceleration with double-sided heating.

### 4.3. Heated wall temperatures

Fig. 10(a)–(c) shows temporal records of the heated wall temperatures for $G$ = 1536.1–1601.3 kg/m$^2$ s for top wall heating, bottom wall heating, and double-sided heating during the CHF transient for highly subcooled ($\Delta T_{sub,in}$ = 24.5–25 °C), slightly subcooled ($\Delta T_{sub,in}$ = 3.3–5.0 °C), and saturated ($x_{e,in}$ = 0.03–0.04) inlet conditions, respectively. The $x$-axis in these plots indicates the time in seconds starting the instant the last heat flux increment that culminated in CHF is initiated. As discussed earlier, power input to the heaters is automatically cut off once any of the relay thermocouples exceeds 130 °C. A common trend observed for most cases and all three heating configurations is temperatures increasing from the leading edge of the heated wall ($T_{w1,1}$, $T_{w2,1}$) to a maximum immediately downstream from the middle ($T_{w1,5}$ or $T_{w1,6}$, $T_{w2,5}$ or $T_{w2,6}$), before decreasing again toward the exit ($T_{w1,7}$, $T_{w2,7}$). This trend is explained in a previous study by the authors [23] as the result of flow acceleration and increased vapor layer thickness on heat transfer. Fig. 10(a) shows CHF is triggered over a much shorter time span for high inlet subcooling of $\Delta T_{sub,in}$ = 24.5–25 °C compared to both slightly subcooled inlet, Fig. 10(b), and saturated inlet, Fig. 10(c).

### 4.4. Heat transfer coefficients

The local heat transfer coefficient at a thermocouple location along a heated wall is obtained from the relation

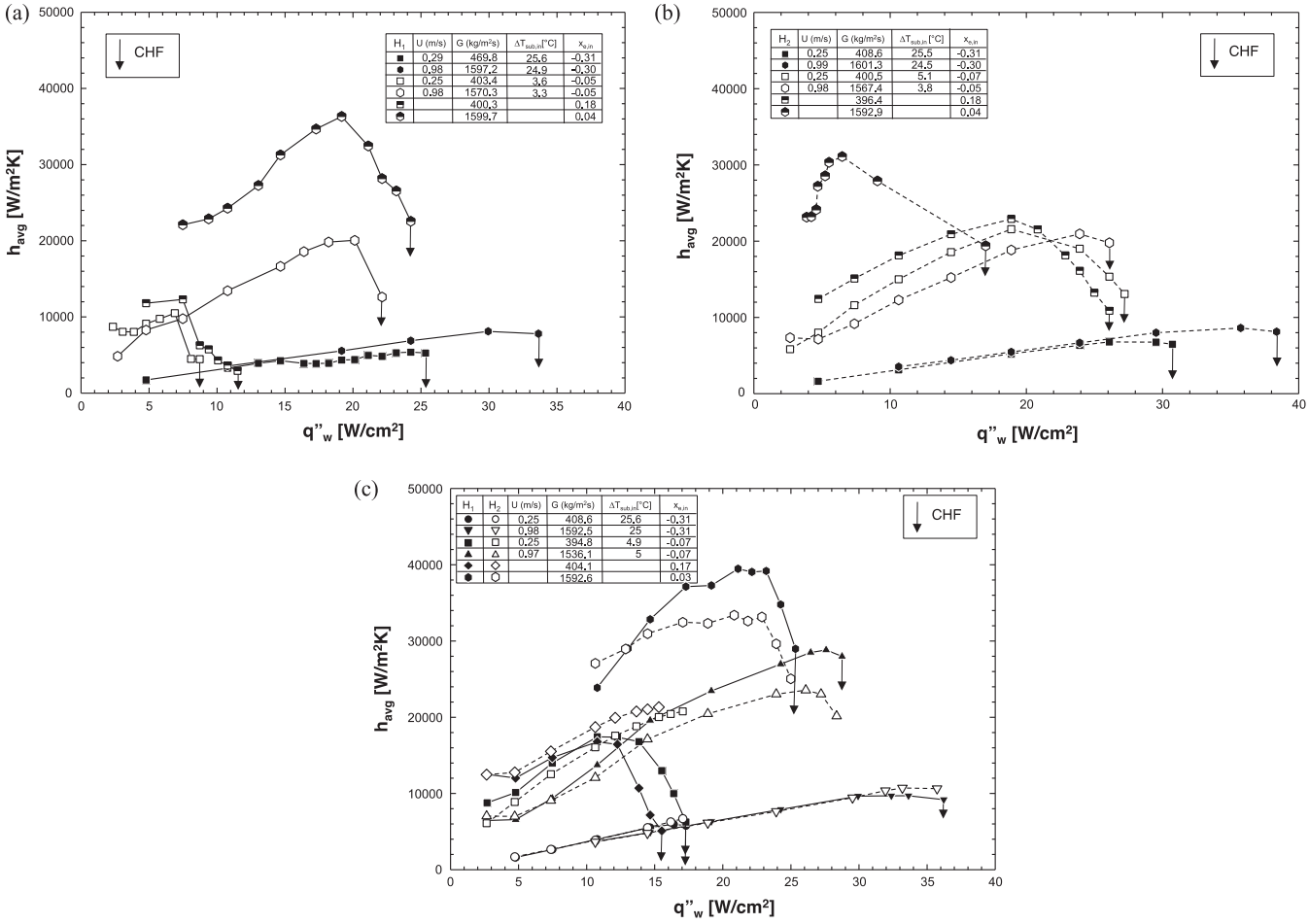


**Fig. 11.** Variations of average heat transfer coefficient with wall heat flux for different inlet mass velocities, inlet subcoolings, and inlet qualities for (a) top wall heating, (b) bottom wall heating, and (c) double-sided heating.

$$h_{m,n} = \frac{q''_w}{(T_{wm,n} - T_f)}, \quad (1)$$

where $q''_w$ is the wall heat flux, $T_{wm,n}$ the wall temperature measured along heated wall $m$ ($m$ = 1 for $H1$ and 2 for $H2$), $n$ the thermocouple location, and $T_f$ the bulk fluid temperature. For double-sided heating, the bulk fluid temperatures for the subcooled and saturated regions are given, respectively, by

$$T_{f,n+1} = T_{f,n} + \frac{(q''_{w1} + q''_{w2})W\Delta z}{\dot{m}c_{p,f}} \quad \text{for } x_e < 0, \quad (2a)$$

and

$$T_f = T_{sat} \quad \text{for } 0 \le x_e \le 1. \quad (2b)$$

The above equations are also used for single-sided heating by setting $q''_{w1}$ = 0 for bottom wall heating, or $q''_{w2}$ = 0 for top wall heating. A single value of the heat transfer coefficient is determined for each thermocouple location, and the values for all thermocouples along a heated wall are then spatially averaged to determine $h_{avg}$.

Fig. 11(a)–(c) shows the variations of $h_{avg}$ with $q''_w$ for $G$ = 394.8–1601.3 kg/m$^2$ s and $\Delta T_{sub,in}$ = 0–25.6 °C and $x_{e,in}$ = −0.31 to 0.18, for top wall heating, bottom wall heating, and double-sided heating, respectively. For top wall heating, Fig. 11(a) shows $h_{avg}$ increases with increasing $G$ for each set of inlet conditions. For $\Delta T_{sub,in}$ = 24.9–25.6 °C, the variation of $h_{avg}$ with $q''_w$ is rather subdued. For $\Delta T_{sub,in}$ = 3.3–3.6 °C and $x_{e,in}$ = 0.04–0.18, $h_{avg}$ increases to a peak value, and then decreases until CHF is reached. For $x_{e,in}$ = 0.04–0.18, $h_{avg}$ is substantially higher than for $\Delta T_{sub,in}$ = 24.9–25.6 °C. This difference can be explained by the highly subcooled flow inhibiting bubble nucleation along the heated length, which compromises heat transfer effectiveness. Fig. 11(b) and (c) shows fairly similar trends of $h_{avg}$ versus $q''_w$ for bottom wall heating and double-sided heating, respectively. Overall, Fig. 11(a)–(c) shows that the influence of $G$ on $h_{avg}$ is relatively small for highly subcooled inlet, more significant for slightly subcooled inlet, and quite substantial for saturated inlet. For top wall heating and double-sided heating, the influence of $G$ on $h_{avg}$ is apparent for both slightly subcooled and saturated inlet cases, while for bottom heating, this influence is limited to saturated inlet cases only. The variations of $h_{avg}$ with $q''_w$ for double-sided heating in Fig. 11(c) bare some similarity to the variations of respective individually heated top wall, Fig. 11(a), and bottom wall, Fig. 11(b), though overall heat transfer performance is higher than for single-sided heating. Comparing these trends with those for CHF in Fig. 8(a)–(c) shows that increasing subcooling enhances CHF but decreases $h_{avg}$ significantly.

Thus far, double-sided heating appears to combine the effects of single-sided heating configurations. To further explore this trend, it is useful to examine the axial variations of the local heat transfer coefficient, $h$, for the double-sided heating. Fig. 12(a)–(c) shows these variations for $G$ = 1536.3–1592.6 kg/m$^2$ s for high subcooled inlet ($\Delta T_{sub,in}$ = 25 °C), slightly subcooled inlet ($\Delta T_{sub,in}$ = 5.0 °C), and saturated inlet ($x_{e,in}$ = 0.03), respectively. For $\Delta T_{sub,in}$ = 25 °C, Fig. 12(a) shows the variation of $h$ with $z$ is rather flat, but shifted

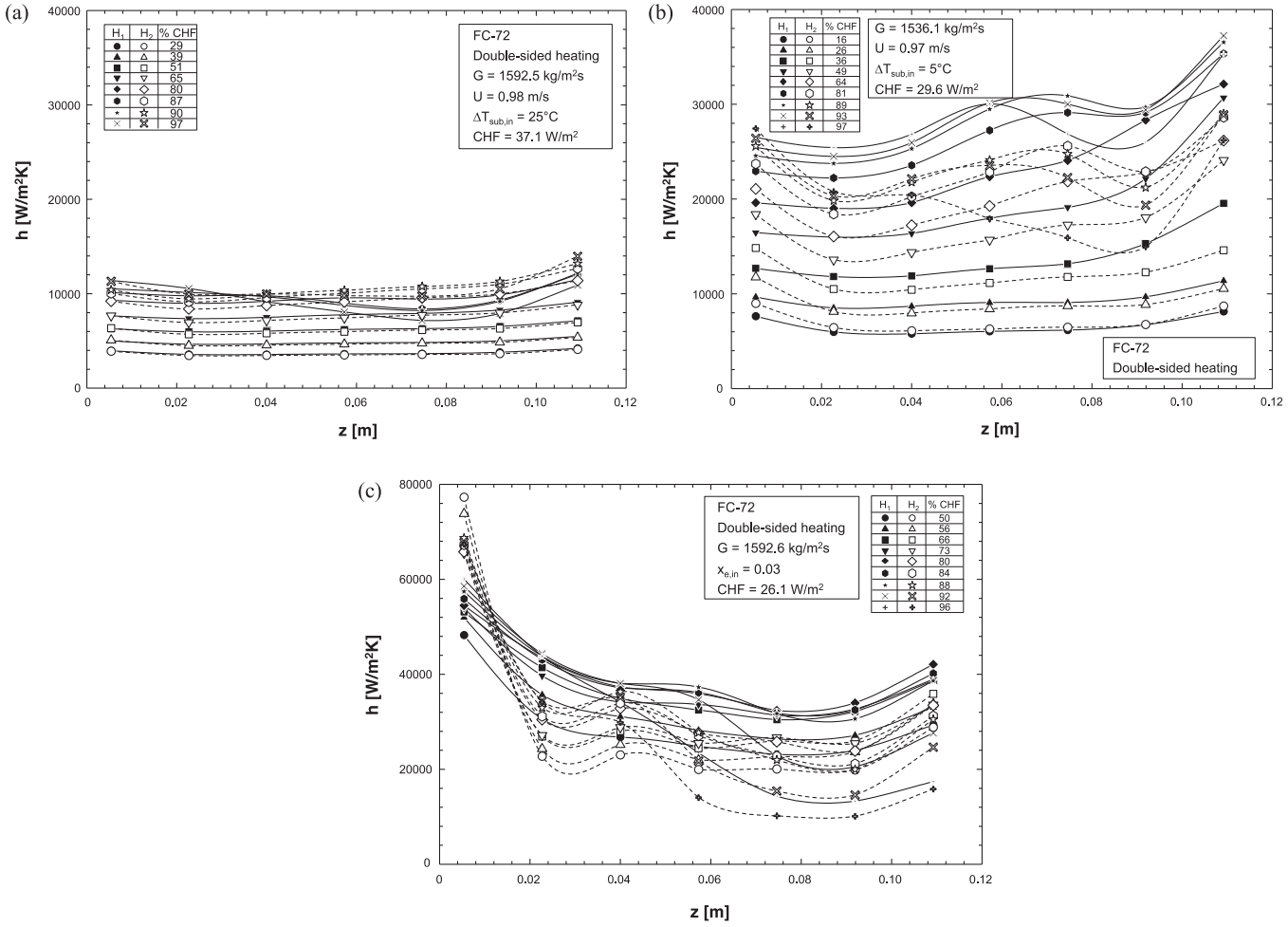


**Fig. 12.** Variations of local heat transfer coefficient along the channel for double-sided heating with increasing heat flux for $G$ = 1536.1–1592.6 kg/m$^2$ s and (a) $\Delta T_{sub,in}$ = 25 °C, (b) $\Delta T_{sub,in}$ = 5 °C, and (c) $x_{e,in}$ = 0.03.

upwards with increasing $q''_w$. For $\Delta T_{sub,in}$ = 5 °C, Fig. 12(b) shows a similarly flat variation of $h$ with $z$ for low heat fluxes. And while there is an upwards shift with increasing $q''_w$, there are appreciable axial variations in $h$ for high heat fluxes, especially close to CHF. These spatial variations are the result of wavy vapor layer formation and development along the channel.

For saturated inlet with $x_{e,in}$ = 0.03, Fig. 12(c) shows variations of $h$ with $z$ for heat fluxes ranging from 50% CHF to 96% CHF. Here, $h$ is highest at the inlet to the heated portion of the channel and decreases appreciably with $z$ before increasing again downstream. The upstream decrease is apparently the result of appreciable thickening of the incoming vapor layers along both walls due to vapor generation by heating. However, $h$ begins to increase downstream due to intensified flow acceleration brought about by the vapor production. Fig. 12(c) also shows $h$ increasing with increasing $q''_w$ up to 73% CHF, because of the benefits of added flow acceleration, and decreasing as CHF is approached as the detrimental effects of thicker insulating vapor layers begin to outweigh the merits of acceleration.

Fig. 13(a)–(c) shows the variations of $h$ with $z$ for double-sided heating and different mass velocities for high subcooled inlet ($\Delta T_{sub,in}$ = 25–27.4 °C), slightly subcooled inlet ($\Delta T_{sub,in}$ = 4.9–6.7 °C), and saturated inlet ($x_{e,in}$ = 0.03–0.17), respectively. The values of wall heat flux in these figures correspond to those that yield peak $h_{avg}$ values as depicted earlier in Fig. 11(a)–(c). In Fig. 13(a), the variation of $h$ with $z$ for $\Delta T_{sub,in}$ = 25–27.4 °C is rather flat and shifted upwards with increasing $G$. For $\Delta T_{sub,in}$ = 4.9–6.7 °C, Fig. 13(b) shows $h$ values increase appreciably compared to those in Fig. 13(a), but the axial variations are more complex, reflecting the aforementioned effects of both vapor layer development and flow acceleration. For $x_{e,in}$ = 0.03–0.17, Fig. 13(c) shows improvement in overall heat transfer performance, with the highest $h$ occurring at the upstream edge, and downstream variations reflecting both vapor layer development and flow acceleration effects. One notable trend in Fig. 13(c) is the significant difference in heat transfer performance between the top and bottom heating walls at the leading edge for $G$ = 404.1 kg/m$^2$ s. This trend can be attributed to the combined effects of incoming vapor and strong buoyancy accumulating vapor mostly against the top wall for this low mass velocity. Fig. 13(a) and (c) shows that heat transfer for $\Delta T_{sub,in}$ = 25–27.4 °C and $x_{e,in}$ = 0.03–0.17, respectively, is enhanced with increasing mass velocity. However, for $\Delta T_{sub,in}$ = 4.9–6.7 °C, Fig. 13(b) shows heat transfer performances for $G$ = 1536.1 kg/m$^2$ s ($U$ = 0.97 m/s) and $G$ = 3211.6 kg/m$^2$ s ($U$ = 2.04 m/s) are quite close. As explained by the authors in a previous study [23], this apparent anomaly can be explained as follows. For low inlet subcooling, there is a trade-off when comparing heat transfer results for different mass velocities at the same wall heat flux, where a lower velocity yields higher vapor void, especially downstream, offsetting the benefits of higher velocity. The absence of this anomaly for $\Delta T_{sub,in}$ = 25–27.4 °C, Fig. 13(a), and $x_{e,in}$ = 0.03–0.17, Fig. 13(c), points to the complexity of assessing the combined influence of inlet quality and mass velocity on heat transfer and CHF.

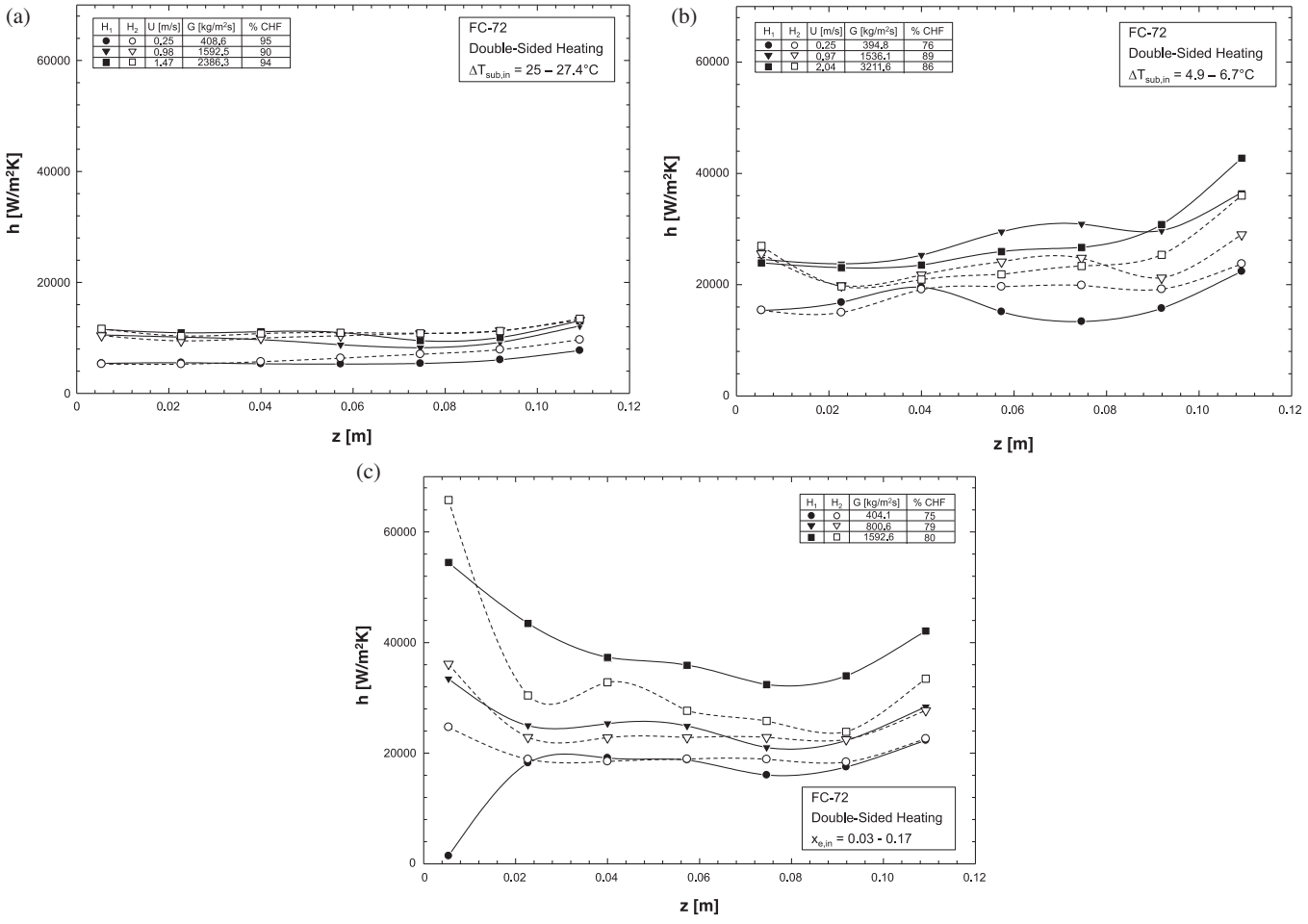


**Fig. 13.** Variations of local heat transfer coefficient along the channel for double-sided heating and different mass velocities for (a) $\Delta T_{sub,in}$ = 25–27.4 °C, (b) $\Delta T_{sub,in}$ = 4.9–6.7 °C, and (c) $x_{e,in}$ = 0.03–0.17.

### 4.5. Effects of subcooling on CHF

A series of prior studies by Galloway and Mudawar [34,35], and Sturgis and Mudawar [24,25] have culminated in a theoretical *Interfacial Lift-off Model* for flow boiling CHF corresponding to zero subcooling that yields

$$CHF_{sat} = b\rho_g h_{fg}\left[\left(\frac{4\pi\sigma\delta}{\rho_g b\lambda_c^2}\sin(\pi b)\right)\Big|_{z^*}\right]^{1/2}, \quad (3)$$

where $b$, $\delta$ and $\lambda_c$, are, respectively, the ratio of wetting front length to wavelength, mean vapor layer thickness, and critical wavelength, all determined at axial location $z^*$ (extent of upstream wetting front) using a two-phase slip flow model. The same model was later proven by Zhang et al. to be highly effective at predicting CHF for different flow orientation relative to Earth gravity [36] as well as for flow boiling in microgravity [33]. Zhang et al. [19] later extended this model to highly subcooled conditions according to

$$CHF_{sub} = \frac{b}{\varepsilon}\rho_g(h_{fg} + c_{pf}\Delta T_{sub,out})\left[\left(\frac{4\pi\sigma\delta}{\rho_g b\lambda_c^2}\sin(\pi b)\right)\Big|_{z^*}\right]^{1/2}, \quad (4)$$

where $\Delta T_{sub,out}$ is the outlet subcooling, and $\varepsilon$ the heat utility ratio. Two key criteria concerning the magnitude of this parameter are $0 \leqslant \varepsilon \leqslant 1$ for subcooled flow, and $\varepsilon = 1$ for saturated flow. Zhang et al. [19] developed the following empirical relation for $\varepsilon$,

$$\varepsilon = 1 - 0.00285\frac{\rho_f}{\rho_g}\frac{c_{pf}\Delta T_{sub,out}}{h_{fg}}\left(\frac{\rho_f U^2 D}{\sigma}\right)^{0.2}, \quad (5)$$

where $D$ is the channel's hydraulic diameter.

Fig. 14(a) shows the variation of heat utility ratio according to Eq. (5) for $U = 0.25$, 0.5, 1 and 1.5 m/s, and a saturation pressure of 150 kPa. The heat utility ratio has a value of $\varepsilon = 1$ for $\Delta T_{sub,out} = 0$, and decreases with increasing subcooling. From Eq. (4), it is evident that CHF increases with decreasing $\varepsilon$, *i.e.*, with increasing subcooling. Fig. 14(a) shows a 20–45% decrease in $\varepsilon$ at 30 °C subcooling, depending on flow velocity. This behavior is consistent with the trend of CHF increasing monotonically with increasing subcooling (albeit inlet rather than outlet) captured in Fig. 8(c) for the present data. Another important trend that is manifest in Fig. 14(a) is the steepening of negative slope of $\varepsilon$, or positive slope for CHF, with increasing velocity, a trend also captured in Fig. 8(c) for bottom wall heating and double-sided heating, but not top wall heating. This is a reflection of the fact that the influence of heat utility ratio on CHF according to Eqs. (4) and (5) is intended to account for the effects of subcooling and velocity but not gravity [19]. For top wall heating, CHF is highly influenced by gravity for low velocity and inertia for high velocity, which leads to a less than monotonic variation of CHF versus velocity. The complex influence of gravity on CHF for subcooled inlet conditions was recently explored by the present authors [23] in regards to the role of interfacial instability in assessing the competing roles of gravity and inertia for the three heating configurations shown in Fig. 1(a)–(c).

Dividing the expression for CHF for subcooled outlet conditions, Eq. (4), by the expression for zero outlet subcooling, Eq. (3), and substituting the expression for $\varepsilon$, Eq. (5), yields the dimensionless relation

$$\frac{CHF_{sub}}{CHF_{sat}} = \frac{\left[1 + \frac{c_{pf}\Delta T_{sub,out}}{h_{fg}}\right]}{1 - 0.00285\frac{\rho_f}{\rho_g}\frac{c_{pf}\Delta T_{sub,out}}{h_{fg}}\left(\frac{\rho_f U^2 D}{\sigma}\right)^{0.2}}. \quad (6)$$

Using pairs of inlet subcooling conditions with the same flow velocity for each of the three heating configurations, Fig. 14(b) compares the measured CHF ratio for subcooled flow to saturated flow at the exit with predictions according to Eq. (6). Note that the curves for top wall heating and bottom wall heating in Fig. 14(b) overlap. Overall, the measured trends are similar to those predicted by Eq. (6), however, the predictions show measureable divergence from the data that increases with increasing subcooling. Better predictions are achieved with top wall heating compared to both bottom wall and double-sided heating.

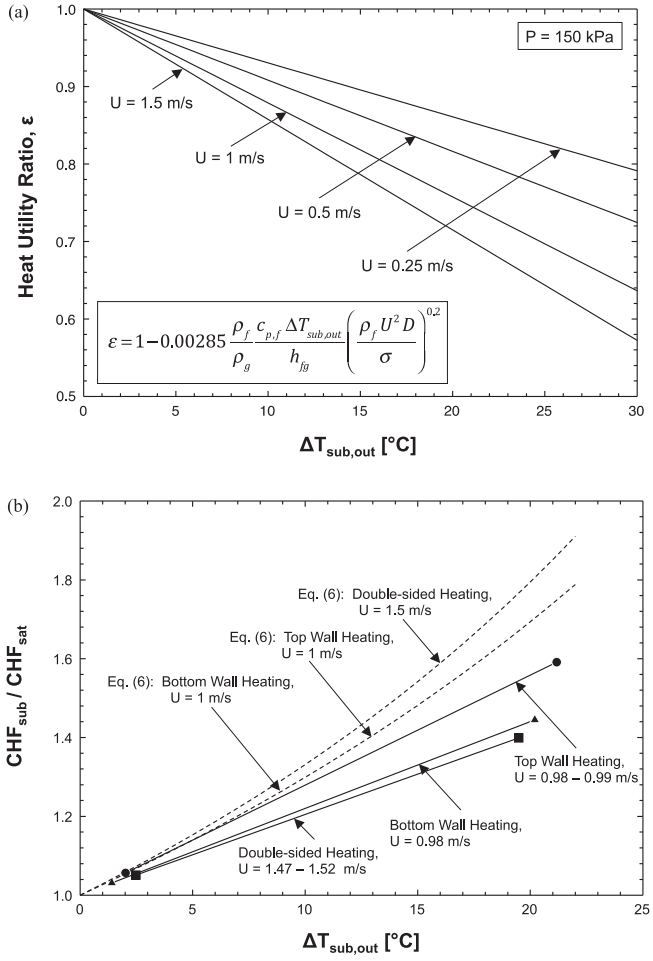


**Fig. 14.** (a) Variation of heat utility ratio with outlet subcooling for $U = 0.25$–1.5 m/s, and (b) comparison of CHF ratio of subcooled outlet to saturated outlet with experimental data.

Future studies with more extensive data may both refine this comparison and yield more accurate correlations that are heating configuration dependent. These endeavors must take advantage of sophisticated instrumentation methods to measure local liquid velocity [37] as well as interface location and temperature distribution across the channel [38].

## 5. Conclusions

This study explored the influence of inlet subcooling and two-phase inlet on flow boiling and CHF in a rectangular channel for top wall heating, bottom wall heating and double-sided heating configurations. FC-72 was used as a working fluid with three inlet conditions: highly subcooled liquid ($\Delta T_{sub,in} = 24.5$–31 °C), slightly subcooled liquid ($\Delta T_{sub,in} = 3.3$–7.7 °C), and saturated two-phase mixture ($x_{e,in} = 0.03$–0.18) for mass velocities of $G = 205.1$–3211.6 kg/m$^2$ s. High-speed video imaging was also used to identify dominant interfacial characteristics for different combinations of inlet conditions and heating configurations. Key findings from the study are as follows.

(1) Overall, gravity plays a dominant role on interfacial behavior for low mass velocities around 400 kg/m$^2$ s. This role is manifest in vapor removal from the bottom wall and vapor accumulation along the top wall. For mass velocities around 1600 kg/m$^2$ s, inertia takes over, leading to formation of similar wavy vapor layers along the top and bottom walls when heated individually, and to double-sided heating appearing as a superposition of vapor layer behaviors observed in the single-sided heating configurations.
(2) Highly subcooled inlet produces a wavy vapor layer along the top wall for low mass velocities compared to thin vapor layers confined to the heated walls at high mass velocities. For slightly subcooled inlet, a higher rate of vapor generation is observed with distinct wavy vapor layers generated along the heated walls. Saturated two-phase inlet results in a complicated flow pattern due to interaction of vapor entering the channel with the vapor generation by heating.
(3) The average heat transfer coefficient increases with increasing heat flux to a peak value before degrading as CHF is approached. Heat transfer is improved significantly as inlet conditions are changed from highly subcooled to slightly subcooled to saturated. The local heat transfer coefficient is fairly flat along the heating wall for highly subcooled inlet, exhibits spatial fluctuations for slightly subcooled inlet because of flow acceleration and vapor accumulation, and decreases from peak value at the upstream edge for saturated inlet.
(4) Overall, CHF increases considerably with increasing inlet subcooling. Bottom wall heating provides the best performance for gravity-dominated low velocity conditions, while double-sided heating outperforms both top wall and bottom wall heating for inertia-dominated high velocity conditions.
(5) Despite some divergence between predicted and measured CHF values at high subcooling, heat utility ratio provides an effective means for assessing the influence of inlet subcooling on CHF.

## Conflict of interest

The authors declare that there are no conflicts of interest.

## Acknowledgements

The authors are grateful for the support of this project by the National Aeronautics and Space Administration (NASA) under Grant No. NNX13AB01G. Support was also provided by the NASA Office of the Chief Technologist's Space Technology Research Fellowship Grant No. NNX11AM81H. The authors thank David F. Chao, James D. Wagner, Rochelle I. May, Daniel M. Hauser and Bruce J. Frankenfield of the NASA Glenn Research Center for their technical assistance.

## References

[1] I. Mudawar, Two-phase micro-channel heat sinks: theory, applications and limitations, J. Electronic Packaging – Trans. ASME 133 (2011) 041002.
[2] P.J. Marto, V.J. Lepere, Pool boiling heat transfer from enhanced surfaces to dielectric fluids, J. Heat Transfer – Trans. ASME 104 (1982) 292–299.
[3] I. Mudawar, T.M. Anderson, Optimization of extended surfaces for high flux chip cooling by pool boiling, J. Electronic Packaging – Trans. ASME 115 (1993) 89–100.
[4] H.J. Lee, S.Y. Lee, Heat transfer correlation for boiling flows in small rectangular horizontal channels with low aspect ratios, Int. J. Multiphase Flow 27 (2001) 2043–2062.
[5] S. Mukherjee, I. Mudawar, Smart pumpless loop for micro-channel electronic cooling using flat and enhanced surfaces, IEEE Trans. – CPMT: Compon. Packaging Technol. 26 (2003) 99–109.
[6] J. Lee, I. Mudawar, Low-temperature two-phase micro-channel cooling for high-heat-flux thermal management of defense electronics, IEEE Trans. – CPMT: Compon. Packaging Technol. 32 (2009) 453–465.
[7] M. Monde, T. Inoue, Critical heat flux in saturated forced convective boiling on a heated disk with multiple impinging jets, J. Heat Transfer – Trans. ASME 113 (1991) 722–727.
[8] D.C. Wadsworth, I. Mudawar, Enhancement of single-phase heat transfer and critical heat flux from an ultra-high-flux-source to a rectangular impinging jet of dielectric liquid, J. Heat Transfer – Trans. ASME 114 (1992) 764–768.
[9] D.D. Hall, I. Mudawar, Experimental and numerical study of quenching complex-shaped metallic alloys with multiple, overlapping sprays, Int. J. Heat Mass Transfer 38 (1995) 1201–1216.
[10] L. Lin, R. Ponnappan, Heat transfer characteristics of spray cooling in a closed loop, Int. J. Heat Mass Transfer 46 (2003) 3737–3746.
[11] M. Visaria, I. Mudawar, Theoretical and experimental study of the effects of spray orientation on two-phase spray cooling and critical heat flux, Int. J. Heat Mass Transfer 51 (2008) 2398–2410.
[12] M.K. Sung, I. Mudawar, Experimental and numerical investigation of single-phase heat transfer using a hybrid jet-impingement/micro-channel cooling scheme, Int. J. Heat Mass Transfer 49 (2006) 682–694.
[13] D.D. Hall, I. Mudawar, Ultra-high critical heat flux (CHF) for subcooled water flow boiling – II. High-CHF database and design parameters, Int. J. Heat Mass Transfer 42 (1999) 1429–1456.
[14] F.P. Chiaramonte, J.A. Joshi, Workshop on critical issues in microgravity fluids, transport, and reaction processes in advanced human support technology – final report, NASA TM-2004-212940, 2004.
[15] The National Academies, Recapturing a Future for Space Exploration: Life and Physical Sciences Research for a New Era, National Academies Press, Washington, DC, 2011.
[16] C. Konishi, I. Mudawar, Review of flow boiling and critical heat flux in microgravity, Int. J. Heat Mass Transfer 80 (2015) 469–493.
[17] H. Ohta, Experiments on microgravity boiling heat transfer by using transparent heaters, Nucl. Eng. Des. 175 (1997) 167–180.
[18] Y. Ma, J.N. Chung, An experimental study of critical heat flux (CHF) in microgravity forced-convection boiling, Int. J. Multiphase Flow 27 (2001) 1753–1767.
[19] H. Zhang, I. Mudawar, M.M. Hasan, CHF model for subcooled flow boiling in Earth gravity and microgravity, Int. J. Heat Mass Transfer 50 (2007) 4039–4051.
[20] H. Zhang, I. Mudawar, M.M. Hasan, Assessment of dimensionless CHF correlations for subcooled flow boiling in microgravity and reduced gravity, Int. J. Heat Mass Transfer 50 (2007) (2007) 4568–4580.
[21] C. Konishi, H. Lee, I. Mudawar, M.M. Hasan, H.K. Nahra, N.R. Hall, J.D. Wagner, R.L. May, J.R. Mackey, Flow boiling in microgravity: Part 1 – Interfacial behavior and experimental heat transfer results, Int. J. Heat Mass Transfer 81 (2015) 705–720.
[22] C. Konishi, H. Lee, I. Mudawar, M.M. Hasan, H.K. Nahra, N.R. Hall, J.D. Wagner, R.L. May, J.R. Mackey, Flow boiling in microgravity: Part 2 – Critical heat flux interfacial behavior, experimental data, and model, Int. J. Heat Mass Transfer 81 (2015) 721–736.
[23] C. Kharangate, L. O'Neill, I. Mudawar, M.M. Hasan, H.K. Nahra, R. Balasubramaniam, N.R. Hall, A.M. Macner, J.R. Mackey, Flow boiling and critical heat flux in horizontal channel with one-sided and double-sided heating, Int. J. Heat Mass Transfer 90 (2015) 323–338.
[24] J.C. Sturgis, I. Mudawar, Critical heat flux in a long, rectangular channel subjected to one-sided heating – I. Flow visualization, Int. J. Heat Mass Transfer 42 (1999) 1835–1847.
[25] J.C. Sturgis, I. Mudawar, Critical heat flux in a long, rectangular channel subjected to one-sided heating – II. Analysis of CHF data, Int. J. Heat Mass Transfer 42 (1999) 1849–1862.
[26] C.R. Kharangate, I. Mudawar, M.M. Hasan, Photographic study and modeling of critical heat flux in horizontal flow boiling with inlet vapor void, Int. J. Heat Mass Transfer 55 (2012) 4154–4168.
[27] C.R. Kharangate, I. Mudawar, M.M. Hasan, Experimental and theoretical study of critical heat flux in vertical upflow with inlet vapor void, Int. J. Heat Mass Transfer 55 (2012) 360–374.
[28] W.M. Rohsenow, A method of correlating heat transfer data for surface boiling liquids, Trans. ASME 74 (1952) 969–978.
[29] S. Levy, Prediction of the Critical Heat Flux in Forced Convection Flow, GEAP-3961, General Electric Co., San Jose, CA, 1962.
[30] W.R. Gambill, Generalized prediction of burnout heat flux for flowing, subcooled, wetting liquids, Chem. Eng. Prog. Symp. Ser. 59 (1963) 71–87.
[31] B.P. Avksentyuk, Critical feat fluxes with forced flow of subcooled and saturated liquids, Therm. Eng. 35 (1988) 694–697.
[32] M. Siman-Tov, W.R. Gambill, W.R. Nelson, A.E. Ruggles, G.L. Yoder, Thermal-hydraulic correlations for the advanced neutron source reactor fuel element design and analysis, in: Y.A. Hassan, L.E. Hochreiter (Eds.), Nuclear Reactor Thermal-hydraulics, vol. 190, ASME HTD, 1991, pp. 63–78.
[33] H. Zhang, I. Mudawar, M.M. Hasan, Flow boiling CHF in microgravity, Int. J. Heat Mass Transfer 48 (2005) 3107–3188.
[34] J.E. Galloway, I. Mudawar, CHF mechanism in flow boiling from a short heated wall – Part 1. Examination of near-wall conditions with the aid of photomicrography and high-speed video imaging, Int. J. Heat Mass Transfer 36 (1993) 2511–2526.

[35] J.E. Galloway, I. Mudawar, CHF mechanism in flow boiling from a short heated wall – Part 2. Theoretical CHF model, Int. J. Heat Mass Transfer 36 (1993) 2527–2540.
[36] H. Zhang, I. Mudawar, M.M. Hasan, Experimental and theoretical study of orientation effects on flow boiling CHF, Int. J. Heat Mass Transfer 45 (2002) 4463–4478.
[37] W. Qu, I. Mudawar, S.-Y. Lee, S.T. Wereley, Experimental and computational investigation of flow development and pressure drop in a rectangular micro-channel, J. Electron. Packaging – Trans. ASME 128 (2006) 1–9.
[38] T.H. Lyu, I. Mudawar, I., Statistical investigation of the relationship between interfacial waviness and sensible heat transfer to a falling liquid film, Int. J. Heat Mass Transfer 34 (1991) 1451–1464.